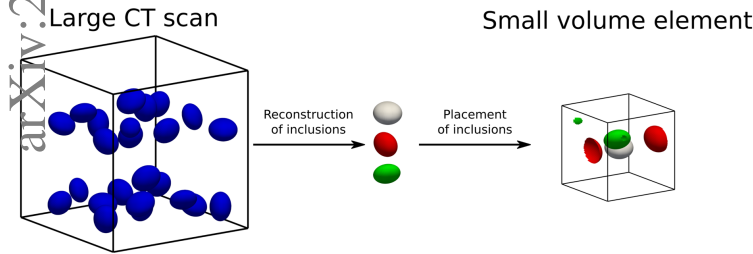


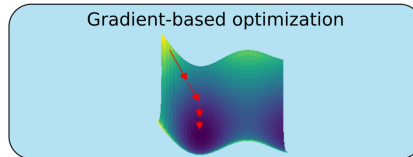
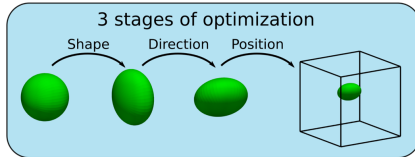
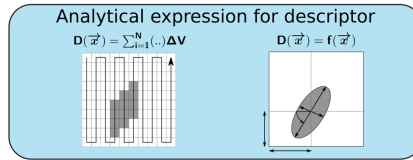
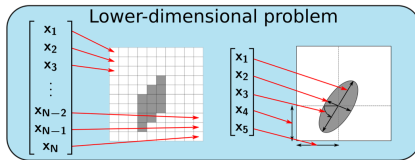
# Graphical Abstract

## Fast reconstruction of microstructures with ellipsoidal inclusions using analytical descriptors

Paul Seibert, Markus Husert, Maximilian P. Wollner, Karl A. Kalina, Markus Kästner



### Key features



## Highlights

### **Fast reconstruction of microstructures with ellipsoidal inclusions using analytical descriptors**

Paul Seibert, Markus Husert, Maximilian P. Wollner, Karl A. Kalina, Markus Kästner

- Analytical expressions for Minkowski functionals and spatial correlations
- Reconstruction from descriptors by efficient gradient-based optimization
- Numerical experiments and discussion of limitations

# Fast reconstruction of microstructures with ellipsoidal inclusions using analytical descriptors

Paul Seibert<sup>a,\*</sup>, Markus Husert<sup>a,\*</sup>, Maximilian P. Wollner<sup>b</sup>, Karl A. Kalina<sup>a</sup> and Markus Kastner<sup>a,c,\*\*</sup>

<sup>a</sup>*Institute of Solid Mechanics, TU Dresden, Dresden, 01069, Germany*

<sup>b</sup>*Institute of Biomechanics, Graz University of Technology, Graz, 8010, Austria*

<sup>c</sup>*Dresden Center for Computational Materials Science, TU Dresden, Dresden, 01069, Germany*

---

## ARTICLE INFO

### Keywords:

microstructure  
characterization  
reconstruction  
differentiable  
descriptor  
gradient-based  
optimization  
simulated annealing  
random heterogeneous media

## ABSTRACT

Microstructure reconstruction is an important and emerging aspect of computational materials engineering and multiscale modeling and simulation. Despite extensive research and fast progress in the field, the application of descriptor-based reconstruction remains limited by computational resources. Common methods for increasing the computational feasibility of descriptor-based microstructure reconstruction lie in approximating the microstructure by simple geometrical shapes and by utilizing differentiable descriptors to enable gradient-based optimization. The present work combines these two ideas for structures composed of non-overlapping ellipsoidal inclusions such as magnetorheological elastomers. This requires to express the descriptors as a function of the microstructure parametrization. Deriving these relations leads to analytical solutions that further speed up the reconstruction procedure. Based on these descriptors, microstructure reconstruction is formulated as a multi-stage optimization procedure. The developed algorithm is validated by means of different numerical experiments and advantages and limitations are discussed in detail.

---

## 1. Introduction

Microstructure characterization and reconstruction (MCR) is an important and emerging field of research on the border between materials science, mechanics and computer science. Harnessing recent hardware developments as well as new algorithms, it aims at accelerating materials engineering by enabling digital workflows such as numerical multiscale simulation [68, 78, 31] and computational (inverse) design [15, 16]. This work presents a new MCR method tailored for materials that are composed of a matrix material with ellipsoidal inclusions. Ellipsoids are often used to approximate inclusions, like in the seminal work by Eshelby [20]. Furthermore, spherical or ellipsoidal particles are often embedded in an elastomer matrix in order to change the effective behavior [6]. Examples comprise glass [19], silica [14] or micron-sized magnetizable [27] particles. The latter are used in magnetorheological elastomers (MREs), which may serve as an exemplary motivation in this work. The microstructure of MREs can be specifically tuned during the production process. For example, chain-like particle distributions [27] or honeycombs [43] can be generated. In face of the high computational cost of magneto-mechanical and other simulations [46, 32], it is promising to use microstructure reconstruction for generating a small, periodic domain from a large, aperiodic volume like a computed tomography scan [71].

A brief introduction on microstructure reconstruction techniques with a focus on recent techniques for random heterogeneous media is given in the following. The reader is referred to the reviews [3, 10, 63] for a more detailed overview. For this purpose, a distinction is made between *descriptor-based* and *data-based* methods. Despite exceptions [40, 61], most methods do not lie in a spectrum between these two extremes, but can clearly be classified into one of these categories.

In data-based methods, a generative model is fitted or trained on a sufficiently large data set of microstructures and is then used to sample new realizations of the same structure. The model types are often inspired by texture synthesis [80] or generative models deep learning and range from local neighborhood-based methods [9, 38, 23] or generative adversarial networks [22, 35, 26], which are sometimes combined with autoencoders [83, 84], to transformers [52]

---

\*Contributed equally

\*\*Corresponding author

ORCID(s): 0000-0002-8774-8462 (P. Seibert); 0000-0001-6170-4069 (K.A. Kalina); 0000-0003-3358-1545 (M. Kastner)

and the recent diffusion models [18, 39]. Much research is focused on identifying suitable model types and adapting them to microstructure reconstruction by enabling 2D-to-3D reconstruction [83, 35] making them applicable to small data sets [18] or ensuring that certain descriptor requirements are met [40, 61].

Descriptor-based methods are not trained on a data set but are given a set of microstructure descriptors and corresponding values. Volume fractions, spatial  $n$ -point correlations [82], the cluster correlation function [29], entropic descriptors [54] and Minkowski functionals [69] are typical candidates. The method of choice depends on the application and two common examples are presented in subsection 2.1. Based on these descriptors, microstructure reconstruction is often but not always [60] formulated as an optimization problem in the space of possible microstructures. For this purpose, the loss function of a microstructure is given by the deviation of the microstructure descriptors from their desired values.

The Yeong-Torquato algorithm [82] is a very well-known descriptor-based reconstruction method, where the optimization problem is directly solved for pixel- or voxel-based microstructures using a specially adapted version of a common stochastic optimizer. Unfortunately, the computational cost of this approach grows extremely at high resolutions and in 3D, where billions of iterations are needed [1]. For this reason, several accelerated approaches have been presented [10]. As an example, with a restricted choice of descriptors, efficient data structures can be employed to compute descriptor updates instead of recomputing the descriptor in every iteration [62, 1]. Furthermore, the sampling rule and acceptance criterion of the pixel swap algorithms have been studied extensively [10] as well as reweighing the cost function [24] and introducing a multigrid scheme [50, 34, 75]. Two ideas that are considered in more detail in the following are (i) low-dimensional microstructure approximations and (ii) differentiable descriptors.

A common method of simplifying the optimization problem is to approximate the structure by simple geometric shapes such as spheres [28]. Ellipsoids, for example, have been used by Xu et al. [81] and Scheunemann et al [65, 64]. For generic shapes, it is recently proposed to combine overlapping circles or spheres to represent complex 2D and 3D shapes [47]. In that work, however, the main focus lies on fitting all inclusions in a volume without overlapping, whereas descriptors are disregarded. This is also a major difficulty with fiber composites, which are commonly approximated by rounded cylinders and are reconstructed from low-dimensional descriptors such as volume fraction and length distribution [66, 44]. Finally, for metallic materials, a structure is often created and parameterized by a Voronoi or Laguerre tessellation. Examples include various codes such as *DREAM.3D* [25], *Kanapy* [55], *NEPER* [56] and *TOP* [37]. Generally, such microstructure approximations are beneficial because they immensely reduce the dimensionality of the optimization problem as compared to a pixel- or voxel-based microstructure representation.

Alternatively, without any approximations to the microstructure morphology, differentiable descriptors can be used to solve the underlying optimization problem using a gradient-based optimizer. This has been presented as differentiable microstructure characterization and reconstruction (DMCR) [72, 73, 75] and various approaches can be identified as special cases [40, 8, 7]. Furthermore, the publicly available *MCRpy* package [74] implements DMCR as well as the Yeong-Torquato algorithm.

The central idea of the present work is that low-dimensional microstructure approximations and differentiable descriptors are not mutually exclusive but can be combined in an algorithm that is accelerated by both methods. The difficulty lies in the fact that the descriptors need to be formulated in terms of and differentiable with respect to the low-dimensional microstructure parametrization. Deriving these relations for microstructures composed of non-overlapping ellipsoids is one central contribution of this work. In fact, these derivations lead to semi-analytical solutions for the descriptors that are very efficient to compute, thus providing a third source of speedup. These descriptors are used to formulate microstructure reconstruction as an optimization problem. Similar to previous reconstruction algorithms [53, 61, 23, 75] this optimization is divided into different stages for a further increase in efficiency.

The work is structured as follows. The developed method is presented in section 2. More precisely, the descriptors of choice are presented in subsection 2.1 and the parametrization of the microstructures is laid out in subsection 2.2. Analytical expressions of the descriptors are derived in subsection 2.3. This forms the basis for formulating microstructure reconstruction as a multi-stage gradient-based optimization procedure in subsection 2.4. Numerical experiments are carried out and discussed in section 3 and the results are summarized in section 4.

The following notation is used. Lower- and uppercase bold letters denote tensors of first ( $\mathbf{x}$ ) and second ( $\mathcal{W}_2^{0,2}$ ) order, respectively. In contrast, vectors ( $\underline{\alpha}$ ) and matrices ( $\underline{\underline{\alpha}}$ ) are bold and single and double underlined, respectively. Non-bold quantities are scalars or other symbols. The Einstein summation convention is not used.

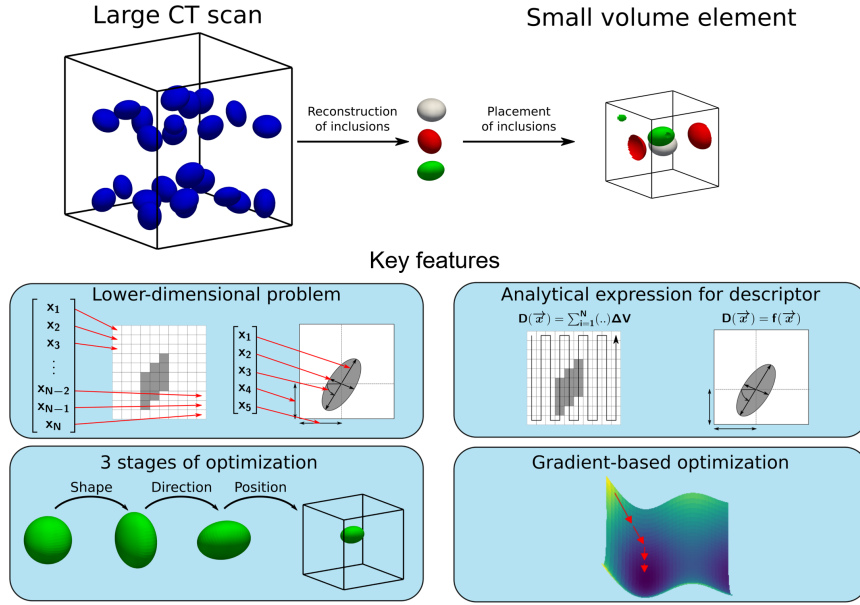


**Figure 1:** Schematic overview of the presented method. A (potentially large) 3D microstructure is characterized by the inclusions' Minkowski functionals and the spatial autocorrelation. From these descriptors, one or many statistical volume elements of arbitrary size can be reconstructed. The algorithm is rendered efficient by (i) the low dimensionality of the optimization problem, (ii) the analytical expressions for the descriptors, (iii) the division of the reconstruction process into multiple stages and (iv) the differentiability of the descriptors, enabling gradient-based optimization.

## 2. Methods

An algorithm for the reconstruction of microstructures from given descriptors is presented in the following. These descriptors, namely the spatial two-point autocorrelation and the Minkowski functionals, are reviewed in subsection 2.1. Very high efficiency is achieved by replacing the often used voxel-based microstructure representation, see *MCRpy* [74], by the degrees of freedom of ellipsoidal inclusions, see Scheunemann et al. [65, 64]. This is outlined in subsection 2.2. Unlike in previous works, these ellipsoids do not overlap. Although distance computation and collision detection cause a significant computational overhead, this allows to directly reconstruct materials where the inclusions cannot overlap for physical reasons, such as magnetorheological elastomers. Furthermore, this allows developing analytical solutions for microstructure descriptors as well as their derivatives, which greatly enhance the efficiency of the method. This derivation is carried out in subsection 2.3. Finally, based on the descriptor formulations, the reconstruction algorithm is formulated as an optimization problem in subsection 2.4. This is summarized in Figure 1.

### 2.1. Descriptors

Minkowski functionals describe the shape of a smooth body in terms of integral values. They are introduced in subsection 2.1.1 and are chosen in the present work for representing individual inclusions. In contrast, the two-point correlation as introduced in subsection 2.1.2 captures information about the spatial distribution of a phase. Here, this accounts for both the shape as well as the relative arrangement of the inclusions. Since the former is already defined by the Minkowski functionals, we use the two-point correlation solely for the positioning of the ellipsoids.

#### 2.1.1. Minkowski functionals

Minkowski functionals are integral measures of the curvature of a smooth body, as such they describe the shape of the inclusions. They can be tensors of arbitrary rank, even zero in the case of scalar functionals. According to Beisbart et al. [5] and Schröder-Turk et al. [69] the general expressions of a Minkowski functional of an inclusion  $\Omega$  are

$$\mathcal{W}_v^{p,q}(\Omega) = \frac{1}{v \binom{d}{v}} \int_{\partial\Omega} S_{v-1}(\kappa_1, \dots, \kappa_{d-1}) \underbrace{\mathbf{x} \otimes \dots \otimes \mathbf{x}}_{p \text{ times}} \otimes \underbrace{\mathbf{n} \otimes \dots \otimes \mathbf{n}}_{q \text{ times}} dS \quad \text{and} \quad (1)$$

$$\mathcal{W}_0^{p,0}(\Omega) = \int_{\Omega} \underbrace{\mathbf{x} \otimes \dots \otimes \mathbf{x}}_{p \text{ times}} d\mathbf{x}. \quad (2)$$

It should be noted that the Minkowski functional  $\mathcal{W}_v^{p,q}$  is not formatted like a tensor, since its tensor rank depends on the values of  $p$  and  $q$  and it may also be a scalar quantity. In the above equation,  $p$ ,  $q$  and  $v$  are indices of the tensor,  $d$  is the dimensionality of the inclusion  $\Omega$ ,  $\mathbf{x}$  and  $\mathbf{n}$  are the position and unit normal vector respectively,  $\kappa_i$  is the  $i$ th principal curvature of the surface,  $dS$  is an infinitesimal surface element and  $S_v(\kappa_1, \dots, \kappa_{d-1})$  is the elementary symmetric function, defined by Schneider [67] for  $v \in \{0, 1, 2\}$  as

$$S_v(\kappa_1, \dots, \kappa_{d-1}) = \begin{cases} 1, & \text{if } v = 0 \\ \sum_{1 \leq j \leq d-1} \kappa_j, & \text{if } v = 1 \\ \sum_{1 \leq i < j \leq d-1} \kappa_i \kappa_j, & \text{if } v = 2 \end{cases}. \quad (3)$$

Herein, the scalar Minkowski functionals of interest are

$$\mathcal{W}_0^{0,0}(\Omega) = \int_{\Omega} d\mathbf{x}, \quad (4)$$

$$\mathcal{W}_1^{0,0}(\Omega) = \frac{1}{3} \int_{\partial\Omega} dS \quad \text{and} \quad (5)$$

$$\mathcal{W}_2^{0,0}(\Omega) = \frac{1}{6} \int_{\partial\Omega} (\kappa_1 + \kappa_2) dS, \quad (6)$$

where  $\mathcal{W}_0^{0,0}$  coincides with the volume and  $\mathcal{W}_1^{0,0}$  with one third of the surface area of the inclusion. Among the tensorial functionals,

$$\mathcal{W}_1^{0,2}(\Omega) = \frac{1}{3} \int_{\partial\Omega} \mathbf{n} \otimes \mathbf{n} dS \quad \text{and} \quad (7)$$

$$\mathcal{W}_2^{0,2}(\Omega) = \frac{1}{6} \int_{\partial\Omega} \mathbf{n} \otimes \mathbf{n} (\kappa_1 + \kappa_2) dS \quad (8)$$

are relevant to this work. They can be interpreted as the normal and curvature distribution, respectively, and more information is given in [70]. It should also be noted that the scalar Minkowski functionals  $\mathcal{W}_1^{0,0}$  and  $\mathcal{W}_2^{0,0}$  correspond to the traces of the tensorial functionals  $\text{tr}(\mathcal{W}_1^{0,2})$  and  $\text{tr}(\mathcal{W}_2^{0,2})$ , respectively.

### 2.1.2. Two-point correlation

The two-point correlation  $S_2^{a \rightarrow b}(\mathbf{r})$  describes the probability of finding the phases  $a$  and  $b$  at the start and end of the vector  $\mathbf{r}$ , if it is placed randomly in the structure. It can be shown that knowledge of one of the four possible two-point correlation, e.g.  $S_2^{1 \rightarrow 1}$ , uniquely determines the remaining three. [48]. For that reason, only the autocorrelation of the inclusion phase

$$S_2^{\text{RVE}}(\mathbf{r}) = S_2^{1 \rightarrow 1} = \frac{1}{V^{\text{RVE}}} \int_{\Omega^{\text{RVE}}} \mathcal{I}(\mathbf{x}) \cdot \mathcal{I}(\mathbf{x} + \mathbf{r}) d\mathbf{x} \quad (9)$$

is considered and hereafter referred to as the two-point correlation. Herein,  $\Omega^{\text{RVE}}$  and  $V^{\text{RVE}}$  denote the domain and the volume of the RVE respectively and  $\mathcal{I}^{\text{RVE}}(\mathbf{x})$  is the indicator-function

$$\mathcal{I}^{\text{RVE}}(\mathbf{x}) = \begin{cases} 1, & \text{if } \mathbf{x} \in \Omega^{\text{incl}} \\ 0, & \text{otherwise} \end{cases}, \quad (10)$$

where the inclusion domain  $\Omega^{\text{incl}}$  is periodically extended beyond the RVE. For this reason,  $\mathcal{I}^{\text{RVE}}(\mathbf{x})$  and  $S_2^{\text{RVE}}(\mathbf{r})$  are also periodic and can be represented as Fourier series

$$S_2^{\text{RVE}}(\mathbf{r}) = \sum_{j=-\infty}^{\infty} \sum_{k=-\infty}^{\infty} \sum_{l=-\infty}^{\infty} \overline{S_{2,jkl}^{\text{RVE}}} e^{i\omega(j,k,l) \cdot \mathbf{r}} \quad \text{and} \quad (11)$$

$$\mathcal{I}^{\text{RVE}}(\mathbf{x}) = \sum_{j=-\infty}^{\infty} \sum_{k=-\infty}^{\infty} \sum_{l=-\infty}^{\infty} \bar{\mathcal{I}}_{jkl}^{\text{RVE}} e^{i\boldsymbol{\omega}(j,k,l)\cdot\mathbf{x}}, \quad (12)$$

with the Fourier coefficients

$$\bar{\mathcal{S}}_{2jkl}^{\text{RVE}} = \bar{\mathcal{S}}_2^{\text{RVE}}(\boldsymbol{\omega}(j, k, l)) = \frac{1}{V^{\text{RVE}}} \int_{\Omega^{\text{RVE}}} \mathcal{S}_2(\mathbf{r}) e^{-i\boldsymbol{\omega}\cdot\mathbf{r}} d\mathbf{r} \quad \text{and} \quad (13)$$

$$\bar{\mathcal{I}}_{jkl}^{\text{RVE}} = \bar{\mathcal{I}}^{\text{RVE}}(\boldsymbol{\omega}(j, k, l)) = \frac{1}{V^{\text{RVE}}} \int_{\Omega^{\text{RVE}}} \mathcal{I}(\mathbf{x}) e^{-i\boldsymbol{\omega}\cdot\mathbf{x}} d\mathbf{x}. \quad (14)$$

In these equations, the frequency vector  $\boldsymbol{\omega}$  is defined as

$$\boldsymbol{\omega}(j, k, l) = 2j \frac{\pi}{l_1} \mathbf{e}_1 + 2k \frac{\pi}{l_2} \mathbf{e}_2 + 2l \frac{\pi}{l_3} \mathbf{e}_3, \quad (15)$$

where  $l_1, l_2$  and  $l_3$  are the side lengths of the RVE.

In practice, the two-point correlation is approximated by truncating the Fourier series expansion after  $\bar{N}_1, \bar{N}_2$  and  $\bar{N}_3$  terms in the three spatial coordinates, respectively, i.e.

$$\tilde{\mathcal{S}}_2^{\text{RVE}}(\mathbf{r}) = \sum_{j=-\bar{N}_1}^{\bar{N}_1} \sum_{k=-\bar{N}_2}^{\bar{N}_2} \sum_{l=-\bar{N}_3}^{\bar{N}_3} \bar{\mathcal{S}}_{2jkl}^{\text{RVE}} e^{i\boldsymbol{\omega}(j,k,l)\cdot\mathbf{r}}. \quad (16)$$

## 2.2. Representation of ellipsoids and microstructures

A single ellipsoid can be represented as

$$\Omega^{\text{ellipsoid}}(\underline{\mathbf{a}}, \underline{\boldsymbol{\alpha}}, \underline{\mathbf{p}}) = \{ \mathbf{x} \in \mathbb{R}^3 \mid (\mathbf{x} - \underline{\mathbf{p}}) \cdot \underbrace{\mathbf{R}(\underline{\boldsymbol{\alpha}}) \cdot \mathbf{A}'(\underline{\mathbf{a}}) \cdot \mathbf{R}(\underline{\boldsymbol{\alpha}})^T}_{\mathbf{A}(\underline{\mathbf{a}}, \underline{\boldsymbol{\alpha}})} \cdot (\mathbf{x} - \underline{\mathbf{p}}) - 1 \leq 0 \}. \quad (17)$$

Herein, the semi-axes  $\underline{\mathbf{a}} = [a_1, a_2, a_3]$  defining its size are sorted by magnitude<sup>1</sup>

$$a_1 > a_2 > a_3 \quad (18)$$

and arranged in a diagonal matrix

$$[\mathbf{A}'_{ij}](\underline{\mathbf{a}}) = \text{diag}(a_1^{-2}, a_2^{-2}, a_3^{-2}) = \begin{bmatrix} a_1^{-2} & 0 & 0 \\ 0 & a_2^{-2} & 0 \\ 0 & 0 & a_3^{-2} \end{bmatrix}. \quad (19)$$

Furthermore,  $\mathbf{R}$  denotes a second order rotation tensor defined by

$$\mathbf{R}(\underline{\boldsymbol{\alpha}}) = \mathbf{R}^x(\alpha_1) \cdot \mathbf{R}^y(\alpha_2) \cdot \mathbf{R}^z(\alpha_3), \quad (20)$$

where the superscript of  $\mathbf{R}$  denotes the axis and the extrinsic Tait-Bryan angles  $\underline{\boldsymbol{\alpha}} = [\alpha_1, \alpha_2, \alpha_3]$  define the rotation angle. Finally, the position vector  $\underline{\mathbf{p}} = p_1 \mathbf{e}_1 + p_2 \mathbf{e}_2 + p_3 \mathbf{e}_3$  defines the center location.

With this representation of a single ellipsoid and an RVE defined as a rectangular domain

$$\Omega^{\text{RVE}} = \{ \mathbf{x} \in \mathbb{R}^3 \mid 0 \leq \mathbf{x} \cdot \mathbf{e}_1 < l_x \text{ and } 0 \leq \mathbf{x} \cdot \mathbf{e}_2 < l_y \text{ and } 0 \leq \mathbf{x} \cdot \mathbf{e}_3 < l_z \}, \quad (21)$$

a microstructure is defined by periodic continuation of all ellipsoids

$$\Omega^{\text{incl.e}}(\underline{\mathbf{a}}, \underline{\boldsymbol{\alpha}}, \underline{\mathbf{p}}) = \bigcup_{i=1}^{N^{\text{incl}}} \bigcup_{j,k,l=-\infty}^{\infty} \Omega^{\text{ellipsoid}}(\underline{\mathbf{a}}^i, \underline{\boldsymbol{\alpha}}^i, \underline{\mathbf{p}}^i + j \cdot l_x \mathbf{e}_1 + k \cdot l_y \mathbf{e}_2 + l \cdot l_z \mathbf{e}_3). \quad (22)$$

Herein, a double underscore notation is introduced for  $\underline{\mathbf{a}}, \underline{\boldsymbol{\alpha}}$  and  $\underline{\mathbf{p}}$  to denote matrices where the  $i$ -th row contains the respective quantity for ellipsoid number  $i$ . Starting with the descriptors introduced in subsection 2.1, this notation allows analytical derivations that are presented in the following in subsection 2.3.

<sup>1</sup>The following derivations assume inequality. In the case of equality, a small value can be added to ensure this condition. Alternatively, the special case could be investigated in a future work.

### 2.3. Analytical derivations of descriptors for structures with ellipsoidal inclusions

Minkowski functionals of single ellipsoids are derived in subsection 2.3.1. The arrangement of multiple ellipsoidal inclusions is described by the two-point autocorrelation, which is derived in subsection 2.3.2.

#### 2.3.1. Minkowski functionals of ellipsoids

Because the considered Minkowski functionals are translation invariant, the ellipsoid is assumed to be located at the origin without loss of generality. Moreover, the coordinate system is aligned with the principal axes of the ellipsoids and a back-transformation to the rotated coordinate system is applied to the Minkowski functionals after integration as

$$\mathcal{W}_v^{0,2}(\underline{\mathbf{a}}, \underline{\boldsymbol{\alpha}}) = \mathbf{R}(\underline{\boldsymbol{\alpha}}) \cdot \mathcal{W}_v^{0,2'}(\underline{\mathbf{a}}) \cdot \mathbf{R}(\underline{\boldsymbol{\alpha}})^T. \quad (23)$$

Due to symmetry reasons, the coordinates of  $\mathcal{W}_v^{0,2'}$  form a diagonal matrix with three independent variables

$$[\mathcal{W}_v^{0,2'}]_{jk}(\underline{\mathbf{a}}) = \begin{bmatrix} \mathcal{W}_v^{0,2'}{}_{11}(\underline{\mathbf{a}}) & 0 & 0 \\ 0 & \mathcal{W}_v^{0,2'}{}_{22}(\underline{\mathbf{a}}) & 0 \\ 0 & 0 & \mathcal{W}_v^{0,2'}{}_{33}(\underline{\mathbf{a}}) \end{bmatrix}. \quad (24)$$

Thus, the tensorial Minkowski functionals  $\mathcal{W}_v^{0,2}$  for  $v \in \{1, 2\}$  are computed in the principal space by explicitly carrying out the integrals given in subsection 2.1.1.

After this, the scalar Minkowski functionals can be obtained.  $\mathcal{W}_0^{0,0}(\underline{\mathbf{a}})$  equals the volume of an ellipsoid,

$$\mathcal{W}_0^{0,0}(\underline{\mathbf{a}}) = \frac{4\pi}{3} a_1 \cdot a_2 \cdot a_3, \quad (25)$$

and is easily defined by the product of its semi-axes. Since the scalar Minkowski functionals

$$\mathcal{W}_v^{0,0}(\underline{\mathbf{a}}) = \text{tr} \left( \mathcal{W}_v^{0,2'}(\underline{\mathbf{a}}) \right) = \sum_{i=1}^3 \mathcal{W}_v^{0,2'}{}_{ii}(\underline{\mathbf{a}}), \quad (26)$$

for  $v \in \{1, 2\}$ , are the traces of their tensorial counterparts, they are rotation invariant and can be calculated as a function of the semi-axes only.

The remainder of this section completes the outlined derivation by carrying out the required integrals. For this purpose, the surface of an unrotated ellipsoid at the coordinate origin  $\partial\Omega^{\text{ellipsoid}'}(\underline{\mathbf{a}})$  is defined in a parametric form by the function

$$\mathbf{x}(\theta, \varphi; \underline{\mathbf{a}}) = a_1 \sin(\theta) \cos(\varphi) \mathbf{e}_1 + a_2 \sin(\theta) \sin(\varphi) \mathbf{e}_2 + a_3 \cos(\theta) \mathbf{e}_3, \quad (27)$$

with the polar angle  $0 \leq \theta \leq \pi$  and the azimuth angle  $0 \leq \varphi \leq 2\pi$ .

In order to calculate the tensorial Minkowski functionals of this surface, the expressions of the surface element  $dS$ , the unit normal vector  $\mathbf{n}$  and the mean curvature  $H$  are derived from the first and second fundamental form of differential geometry. This is carried out explicitly in Appendix A. The integrals in Equation 7 and Equation 8 can be carried out and yield expressions of the tensorial Minkowski functionals of an unrotated ellipsoid

$$\mathcal{W}_1^{0,2'}{}_{11}(\underline{\mathbf{a}}) = \frac{2\pi a_3^2}{3} \beta \cdot \left( -\frac{1}{\gamma - \beta} + \frac{1}{\sqrt{\beta\gamma(1-\beta)}} \left[ \mathcal{F}(\psi, \eta) + \frac{\beta}{\gamma - \beta} \mathcal{E}(\psi, \eta) \right] \right), \quad (28)$$

$$\mathcal{W}_1^{0,2'}{}_{22}(\underline{\mathbf{a}}) = \frac{2\pi a_3^2}{3} \gamma \cdot \left( \frac{1}{\gamma - \beta} + \frac{1}{\sqrt{\beta\gamma(1-\beta)}(1-\gamma)} \left[ \mathcal{F}(\psi, \eta) - \frac{\gamma}{1-\eta} \mathcal{E}(\psi, \eta) \right] \right), \quad (29)$$

$$\mathcal{W}_1^{0,2'}{}_{33}(\underline{\mathbf{a}}) = \frac{2\pi a_3^2}{3} \frac{1}{\sqrt{\beta\gamma(1-\beta)}(1-\gamma)} [-\gamma \mathcal{F}(\psi, \eta) + \mathcal{E}(\psi, \eta)], \quad (30)$$

$$\mathcal{W}_2^{0,2'}{}_{11}(\underline{\mathbf{a}}) = \frac{\pi}{3} a_3 \left( \frac{\zeta}{\sqrt{\delta\zeta}} + \frac{\delta\zeta + \delta - \zeta}{(\delta - \zeta)\sqrt{\delta - 1}} [\mathcal{F}(\psi, \tau) - \mathcal{E}(\psi, \tau)] \right), \quad (31)$$



$$W_{2' 22}^{0,2'}(\underline{\mathbf{a}}) = \frac{\pi}{3(\zeta - 1)} a_3 \left( -\frac{\zeta}{\sqrt{\delta\zeta}} + \frac{\delta - \zeta - \delta\zeta}{\tau\sqrt{\delta - 1}} [(1 - \tau)\mathcal{F}(\psi, \tau) - \mathcal{E}(\psi, \tau)] \right) \quad \text{and} \quad (32)$$

$$W_{2' 33}^{0,2'}(\underline{\mathbf{a}}) = \frac{\pi}{3(\zeta - 1)} a_3 \left( \frac{\zeta^2}{\sqrt{\delta\zeta}} + \frac{\delta\zeta - \delta - \zeta}{\sqrt{\delta - 1}} \mathcal{E}(\psi, \tau) \right), \quad (33)$$

where the substitutions

$$\begin{aligned} \beta &= \left( \frac{a_3}{a_1} \right)^2, \quad \gamma = \left( \frac{a_3}{a_2} \right)^2, \quad \delta = \left( \frac{a_1}{a_3} \right)^2, \quad \zeta = \left( \frac{a_2}{a_3} \right)^2, \\ \eta &= \frac{(1 - \gamma)}{(1 - \beta)}, \quad \tau = \frac{(\delta - \zeta)}{(\delta - 1)} \quad \text{and} \quad \psi = \arccos \left( \frac{a_3}{a_1} \right) \end{aligned} \quad (34)$$

have been made for readability purposes. Furthermore,  $\mathcal{F}$  and  $\mathcal{E}$  denote the incomplete elliptic integrals of the first and second kind, defined by Sidhu [76] as

$$\mathcal{F}(\psi, \eta) = \int_0^\psi \frac{1}{\sqrt{1 - \eta^2 \sin^2(\check{\psi})}} d\check{\psi} \quad \text{and} \quad \mathcal{E}(\psi, \eta) = \int_0^\psi \sqrt{1 - \eta^2 \sin^2(\check{\psi})} d\check{\psi}. \quad (35)$$

### 2.3.2. Spatial correlations of ellipsoid distributions

The spatial autocorrelation can be computed from the indicator function of an RVE, which in turn is composed of indicator functions of individual non-overlapping ellipsoids. Consequently, analytical solutions for the indicator function of single inclusions are derived in Fourier space. These are then aggregated over all ellipsoids and used to compute the spatial autocorrelation.

After defining the indicator function of an ellipsoid  $\mathcal{I}^{\text{ellipsoid}}$  as

$$\mathcal{I}^{\text{ellipsoid}}(\mathbf{x}; \underline{\mathbf{a}}, \underline{\boldsymbol{\alpha}}, \mathbf{p}) = \begin{cases} 1, & \text{if } \mathbf{x} \in \Omega^{\text{ellipsoid}}(\underline{\mathbf{a}}, \underline{\boldsymbol{\alpha}}, \mathbf{p}), \\ 0, & \text{otherwise,} \end{cases} \quad (36)$$

its Fourier transform follows as

$$\begin{aligned} \bar{\mathcal{I}}^{\text{ellipsoid}}(\boldsymbol{\omega}; \underline{\mathbf{a}}, \underline{\boldsymbol{\alpha}}, \mathbf{p}) &= \frac{1}{V^{\text{RVE}}} \int_{\Omega^{\text{RVE}}} \mathcal{I}^{\text{ellipsoid}}(\mathbf{x}; \underline{\mathbf{a}}, \underline{\boldsymbol{\alpha}}, \mathbf{p}) e^{-i\boldsymbol{\omega} \cdot \mathbf{x}} d\mathbf{x} \\ &= \frac{1}{V^{\text{RVE}}} \int_{\Omega^{\text{ellipsoid}}(\underline{\mathbf{a}}, \underline{\boldsymbol{\alpha}}, \mathbf{p})} e^{-i\boldsymbol{\omega} \cdot \mathbf{x}} d\mathbf{x}. \end{aligned} \quad (37)$$

In order to solve the integral over the ellipsoid, it is mapped onto a unit sphere

$$\Omega^{\text{sphere}} = \{\mathbf{x} \in \mathbb{R}^3 \mid |\mathbf{x}| \leq 1\}. \quad (38)$$

This mapping takes the form of

$$\hat{\mathbf{x}} = \mathbf{T} \cdot (\mathbf{x} - \mathbf{p}) \quad \text{and} \quad \mathbf{x} = \mathbf{T}^{-1} \cdot \hat{\mathbf{x}} + \mathbf{p}, \quad (39)$$

with the transformation tensor

$$\mathbf{T}(\underline{\mathbf{a}}, \underline{\boldsymbol{\alpha}}) = \sqrt{\mathbf{A}'}(\underline{\mathbf{a}}) \cdot \mathbf{R}^T(\underline{\boldsymbol{\alpha}}) \quad \text{with} \quad [\sqrt{\mathbf{A}'}_{ij}] (\underline{\mathbf{a}}) = \text{diag}(a_1^{-1}, a_2^{-1}, a_3^{-1}) \quad (40)$$

and  $\hat{\mathbf{x}}$  being the position vector after mapping onto the unit sphere. Applying this transformation to Equation 37 yields

$$\begin{aligned} \bar{\mathcal{I}}^{\text{ellipsoid}}(\boldsymbol{\omega}; \underline{\mathbf{a}}, \underline{\boldsymbol{\alpha}}, \mathbf{p}) &= \frac{1}{\det(\mathbf{T})V^{\text{RVE}}} \int_{\Omega^{\text{sphere}}} e^{-i\boldsymbol{\omega} \cdot (\mathbf{T}^{-1} \cdot \hat{\mathbf{x}} + \mathbf{p})} d\hat{\mathbf{x}} \\ &= \frac{e^{-i\boldsymbol{\omega} \cdot \mathbf{p}}}{\det(\mathbf{T})V^{\text{RVE}}} \int_{\Omega^{\text{sphere}}} e^{-i\boldsymbol{\omega} \cdot \mathbf{T}^{-1} \cdot \hat{\mathbf{x}}} d\hat{\mathbf{x}} \end{aligned}$$

$$\begin{aligned}
 &= \frac{e^{-i\boldsymbol{\omega} \cdot \mathbf{p}}}{\det(\mathbf{T})V^{\text{RVE}}} \int_{r=0}^1 \int_{\varphi=0}^{\pi} \int_{\theta=0}^{2\pi} e^{-i\boldsymbol{\omega} \cdot \mathbf{T}^{-1} \cdot \hat{\mathbf{x}} r^2} \sin(\theta) \, d\varphi \, d\theta \, dr \\
 &= \frac{2\pi e^{-i\boldsymbol{\omega} \cdot \mathbf{p}}}{\det(\mathbf{T})V^{\text{RVE}}} \int_{r=0}^1 \int_{\theta=0}^{\pi} e^{-ir|\boldsymbol{\omega} \cdot \mathbf{T}^{-1}| \cos(\theta)} r^2 \sin(\theta) \, d\theta \, dr.
 \end{aligned} \tag{41}$$

By realizing that

$$\frac{d}{d\theta} e^{-ir|\boldsymbol{\omega} \cdot \mathbf{T}^{-1}| \cos(\theta)} = ir \sin(\theta) |\boldsymbol{\omega} \cdot \mathbf{T}^{-1}| e^{-ir|\boldsymbol{\omega} \cdot \mathbf{T}^{-1}| \cos(\theta)}, \tag{42}$$

the integral over  $\theta$  can be solved:

$$\begin{aligned}
 \overline{\mathcal{I}}^{\text{ellipsoid}}(\boldsymbol{\omega}; \underline{\mathbf{a}}, \underline{\boldsymbol{\alpha}}, \mathbf{p}) &= \frac{2\pi e^{-i\boldsymbol{\omega} \cdot \mathbf{p}}}{\det(\mathbf{T})V^{\text{RVE}}} \int_{r=0}^1 e^{-ir|\boldsymbol{\omega} \cdot \mathbf{T}^{-1}| \cos(\theta)} \Big|_{\theta=0}^{\pi} \frac{r}{i|\boldsymbol{\omega} \cdot \mathbf{T}^{-1}|} \, dr \\
 &= \frac{4\pi e^{-i\boldsymbol{\omega} \cdot \mathbf{p}}}{\det(\mathbf{T})V^{\text{RVE}}} \frac{\sin(|\boldsymbol{\omega} \cdot \mathbf{T}^{-1}|) - |\boldsymbol{\omega} \cdot \mathbf{T}^{-1}| \cos(|\boldsymbol{\omega} \cdot \mathbf{T}^{-1}|)}{|\boldsymbol{\omega} \cdot \mathbf{T}^{-1}|^3}
 \end{aligned} \tag{43}$$

$$\tag{44}$$

By substituting

$$\det(\mathbf{T})(\underline{\mathbf{a}}) = \frac{1}{a_1 a_2 a_3} = \frac{4\pi}{3W_0^{0,0}(\underline{\mathbf{a}})} \quad \text{and} \tag{45}$$

$$\begin{aligned}
 |\boldsymbol{\omega} \cdot \mathbf{T}^{-1}| &= \sqrt{\boldsymbol{\omega} \cdot \mathbf{T}^{-1} \cdot \mathbf{T}^{-T} \cdot \boldsymbol{\omega}} \\
 &= \sqrt{\boldsymbol{\omega} \cdot \mathbf{A}^{-1} \cdot \boldsymbol{\omega}},
 \end{aligned} \tag{46}$$

the following solution is obtained:

$$\begin{aligned}
 \overline{\mathcal{I}}_{jkl}^{\text{ellipsoid}}(\underline{\mathbf{a}}, \underline{\boldsymbol{\alpha}}, \mathbf{p}) &= \overline{\mathcal{I}}^{\text{ellipsoid}}(\boldsymbol{\omega}(j, k, l); \underline{\mathbf{a}}, \underline{\boldsymbol{\alpha}}, \mathbf{p}) = \frac{1}{V^{\text{RVE}}} \int_{\Omega^{\text{ellipsoid}}(\underline{\mathbf{a}}, \underline{\boldsymbol{\alpha}}, \mathbf{p})} e^{-i\boldsymbol{\omega} \cdot \mathbf{x}} \, d\mathbf{x} \\
 &= 3 \cdot \frac{W_0^{0,0}(\underline{\mathbf{a}})}{V^{\text{RVE}}} \cdot e^{-i\boldsymbol{\omega} \cdot \mathbf{p}} \cdot \frac{\sin(\Gamma) - \Gamma \cos(\Gamma)}{\Gamma^3},
 \end{aligned} \tag{47}$$

where  $\Gamma = \sqrt{\boldsymbol{\omega} \cdot \mathbf{A}^{-1}(\underline{\mathbf{a}}, \underline{\boldsymbol{\alpha}}) \cdot \boldsymbol{\omega}}$ .

The Fourier coefficients of an RVE containing  $N^{\text{incl}}$  non-overlapping ellipsoids,  $\overline{\mathcal{I}}_{jkl}^{\text{RVE,e}}$ , can be calculated by summing the coefficients of each ellipsoid due to the linearity of the Fourier transform,

$$\begin{aligned}
 \overline{\mathcal{I}}_{jkl}^{\text{RVE,e}}(\underline{\mathbf{a}}, \underline{\boldsymbol{\alpha}}, \mathbf{p}) &= \overline{\mathcal{I}}^{\text{RVE,e}}(\boldsymbol{\omega}(j, k, l), (\underline{\mathbf{a}}, \underline{\boldsymbol{\alpha}}, \mathbf{p})) \\
 &= \sum_{i=1}^{N^{\text{incl}}} \overline{\mathcal{I}}^{\text{ellipsoid}}(\boldsymbol{\omega}(j, k, l), \underline{\mathbf{a}}^i, \underline{\boldsymbol{\alpha}}^i, \mathbf{p}^i).
 \end{aligned} \tag{48}$$

To obtain an expression for the autocorrelation in Fourier space  $\overline{S}_2^{\text{RVE}}(\boldsymbol{\omega})$ , Equation 9 and Equation 13 are combined

$$\begin{aligned}
 \overline{S}_2^{\text{RVE}}(\boldsymbol{\omega}) &= \frac{1}{V^{\text{RVE}}} \int_{\Omega^{\text{RVE}}} S_2^{\text{RVE}}(\mathbf{r}) e^{-i\boldsymbol{\omega} \cdot \mathbf{r}} \, d\mathbf{r} \\
 &= \frac{1}{(V^{\text{RVE}})^2} \int_{\Omega^{\text{RVE}}} \left[ \int_{\Omega^{\text{RVE}}} \mathcal{I}^{\text{RVE}}(\mathbf{x}) \cdot \mathcal{I}^{\text{RVE}}(\mathbf{x} + \mathbf{r}) \, d\mathbf{x} \right] e^{-i\boldsymbol{\omega} \cdot \mathbf{r}} \, d\mathbf{r} \\
 &= \frac{1}{(V^{\text{RVE}})^2} \int_{\Omega^{\text{RVE}}} \mathcal{I}^{\text{RVE}}(\mathbf{x}) \left[ \int_{\Omega^{\text{RVE}}} \mathcal{I}^{\text{RVE}}(\mathbf{x} + \mathbf{r}) e^{-i\boldsymbol{\omega} \cdot \mathbf{r}} \, d\mathbf{r} \right] \, d\mathbf{x}.
 \end{aligned} \tag{49}$$

Substituting  $\tilde{\mathbf{x}} = \mathbf{x} + \mathbf{r}$  and applying the Wiener-Chintschin theorem yields

$$\begin{aligned}
 \overline{S_2}^{\text{RVE}}(\boldsymbol{\omega}) &= \frac{1}{(V^{\text{RVE}})^2} \int_{\Omega^{\text{RVE}}} \mathcal{I}^{\text{RVE}}(\mathbf{x}) e^{i\boldsymbol{\omega} \cdot \mathbf{x}} \underbrace{\left[ \int_{\Omega^{\text{RVE}}} \mathcal{I}^{\text{RVE}}(\tilde{\mathbf{x}}) e^{-i\boldsymbol{\omega} \cdot \tilde{\mathbf{x}}} d\tilde{\mathbf{x}} \right]}_{V^{\text{RVE}} \overline{\mathcal{I}}^{\text{RVE}}(\boldsymbol{\omega})} d\mathbf{x} \\
 &= \frac{\overline{\mathcal{I}}^{\text{RVE}}}{V^{\text{RVE}}} \underbrace{\int_{\Omega^{\text{RVE}}} \mathcal{I}^{\text{RVE}}(\mathbf{x}) e^{i\boldsymbol{\omega} \cdot \mathbf{x}} d\mathbf{x}}_{V^{\text{RVE}} \cdot (\overline{\mathcal{I}}^{\text{RVE}}(\boldsymbol{\omega}))^*} \\
 &= \overline{\mathcal{I}}^{\text{RVE}}(\boldsymbol{\omega}) \left( \overline{\mathcal{I}}^{\text{RVE}}(\boldsymbol{\omega}) \right)^* = |\overline{\mathcal{I}}^{\text{RVE}}(\boldsymbol{\omega})|^2
 \end{aligned} \tag{50}$$

In the above derivation,  $(\bullet)^*$  denotes the complex conjugate. Also, it should be noted that the shift of the integration domain, which would be required by the substitution  $\tilde{\mathbf{x}} = \mathbf{x} + \mathbf{r}$ , can be neglected since the integrand is periodic with a period length of exactly the RVE side length. For that reason, the above derivation is restricted to the frequency vectors defined in Equation 15. The approximated two-point correlation of an RVE can then be expressed as

$$\tilde{S}_2^{\text{RVE,e}}(\mathbf{r}, \underline{\mathbf{a}}, \underline{\boldsymbol{\alpha}}, \underline{\mathbf{p}}) = \sum_{j=-\overline{N}_1}^{\overline{N}_1} \sum_{k=-\overline{N}_2}^{\overline{N}_2} \sum_{l=-\overline{N}_3}^{\overline{N}_3} \left| \overline{\mathcal{I}}_{jkl}^{\text{RVE,e}}(\underline{\mathbf{a}}, \underline{\boldsymbol{\alpha}}, \underline{\mathbf{p}}) \right|^2 e^{i\boldsymbol{\omega}(j,k,l) \cdot \mathbf{r}}. \tag{51}$$

## 2.4. Reconstruction

The previously derived expressions are used in the following to reconstruct microstructures given the desired descriptors. Following the notation of Scheunemann et al. [65, 64],  $\underline{\boldsymbol{\gamma}}$  is used to denote the parametrization of the microstructure. In the simple and direct case [82, 74],  $\underline{\boldsymbol{\gamma}}$  comprises all pixel or voxel values of the microstructure. In the present work, however,  $\underline{\boldsymbol{\gamma}}$  is given by combining  $\underline{\mathbf{a}}$ ,  $\underline{\boldsymbol{\alpha}}$  and  $\underline{\mathbf{p}}$  as introduced in subsection 2.2 in a single vector. The optimal parametrization often is given by the solution of the optimization problem

$$\underline{\boldsymbol{\gamma}}^{\text{opt}} = \underset{\underline{\boldsymbol{\gamma}}}{\text{argmin}} \mathcal{L}(\underline{\boldsymbol{\gamma}}), \tag{52}$$

where the loss function  $\mathcal{L}$  quantifies the difference between the current and desired descriptor values. In the present case, the optimization problem is decomposed into a two-step procedure

1. Reconstruct a set of ellipsoidal inclusions, where each ellipsoid is characterized by its semi-axes  $\underline{\mathbf{a}}$  and orientations  $\underline{\boldsymbol{\alpha}}$ . The distribution of Minkowski functionals over all inclusions is used for this step.
2. Place the inclusions in the domain under consideration of the spatial two-point autocorrelation. In this step, the ellipsoid shape and orientation remain fixed and only the position vectors are adjusted.

This is shown in algorithm 1 and the individual stages are discussed in subsection 2.4.1 and subsection 2.4.2, respectively. While this approach is not necessarily optimal as given in Equation 52, it is highly efficient and yields very good results<sup>2</sup>.

### 2.4.1. Inclusion reconstruction

Given a set of Minkowski functionals of all inclusions in the original structure

$$\mathbb{W}^{\text{orig}} = \left\{ \left( \mathcal{W}_0^{0,0,\text{orig}}, \mathcal{W}_1^{0,0,\text{orig}}, \mathcal{W}_2^{0,0,\text{orig}}, \mathcal{W}_1^{0,2,\text{orig}}, \mathcal{W}_2^{0,2,\text{orig}} \right)_i \right\}_{i=1}^{N_{\text{orig}}^{\text{incl}}} \tag{53}$$

ellipsoids for an RVE to reconstruct can be sampled by repeatedly drawing tuples of Minkowski functionals until a sufficient number of ellipsoids is reached. The number of ellipsoids is determined by the volume fraction. If the

<sup>2</sup>As a future work, it might be promising to use the present results as an initialization for a convex optimizer for solving the full optimization problem in Equation 52.

**Algorithm 1:** Proposed microstructure reconstruction algorithm.

---

**Input:** Set of original Minkowski functionals  $\mathbb{W}^{\text{orig}}$ ; volume fractions  $v_f$ ; desired autocorrelation  $\tilde{S}_2^{\text{des}}(\mathbf{r})$   
 $N^{\text{incl}} =$  determine from  $\mathbb{W}^{\text{orig}}$  and  $v_f$  // number of inclusions  
// step 1 - reconstructed individual inclusions using Minkowski functionals  
**for**  $i = 1$  **to**  $N^{\text{incl}}$  **do** // loop over inclusions  
     $(\mathcal{W}_0^{0,0}, \mathcal{W}_1^{0,0}, \mathcal{W}_2^{0,0}, \mathcal{W}_1^{0,2}, \mathcal{W}_2^{0,2}) \sim \mathbb{W}^{\text{orig}}$  // sample Minkowski functionals  
     $\underline{\mathbf{a}}^{\text{opt}} = \text{argmin}_{\underline{\mathbf{a}}} \mathcal{L}^{\text{a}}(\underline{\mathbf{a}})$  // find semiaxes, use Eq. (56)  
     $\underline{\boldsymbol{\alpha}}^{\text{opt}} = \text{argmin}_{\underline{\boldsymbol{\alpha}}} \mathcal{L}^{\alpha}(\underline{\mathbf{a}}^{\text{opt}}, \underline{\boldsymbol{\alpha}})$  // find orientation, use Eq. (57)  
**end**  
 $\underline{\mathbf{a}}^{\text{opt}}, \underline{\boldsymbol{\alpha}}^{\text{opt}} = \bigsqcup_{i=1}^{N^{\text{incl}}} \underline{\mathbf{a}}_i^{\text{opt}}, \underline{\boldsymbol{\alpha}}_i^{\text{opt}}$  // assemble over all inclusions  
// step 2 - place inclusions using autocorrelation  
 $\underline{\mathbf{p}}^{\text{opt}} = \text{argmin}_{\underline{\mathbf{p}}} \left[ \mathcal{L}^{\text{p}}(\underline{\mathbf{a}}^{\text{opt}}, \underline{\boldsymbol{\alpha}}^{\text{opt}}, \underline{\mathbf{p}}) + \lambda \cdot \mathcal{L}^{\text{c}}(\underline{\mathbf{a}}^{\text{opt}}, \underline{\boldsymbol{\alpha}}^{\text{opt}}, \underline{\mathbf{p}}) \right]$  // find positions, use Eq. (59) and (60)  
**Output:** Reconstructed microstructure, parameterized by  $\underline{\mathbf{a}}^{\text{opt}}, \underline{\boldsymbol{\alpha}}^{\text{opt}}$  and  $\underline{\mathbf{p}}^{\text{opt}}$

---

reconstructed structure is of smaller or equal size as the original one, tuples of Minkowski functionals can be drawn without replacement, which is denoted by

$$(\mathcal{W}_0^{0,0}, \mathcal{W}_1^{0,0}, \mathcal{W}_2^{0,0}, \mathcal{W}_1^{0,2}, \mathcal{W}_2^{0,2}) \sim \mathbb{W}^{\text{orig}}. \quad (54)$$

This ensures that the set of reconstructed inclusions  $\mathbb{W}^{\text{rec}} \subseteq \mathbb{W}^{\text{orig}}$ . If the original structure is significantly larger, advanced techniques such as stratified sampling may be used [49].

After this sampling is completed, the semiaxes  $\underline{\mathbf{a}}$  and orientation  $\underline{\boldsymbol{\alpha}}$  need to be recovered from the Minkowski functionals. Because the three scalar Minkowski functionals are rotation-invariant, they are used to determine  $\underline{\mathbf{a}}$ , whereas  $\underline{\boldsymbol{\alpha}}$  follow from their tensorial counterparts. For this purpose, two distinct optimization problems,

$$\underline{\mathbf{a}}^{\text{opt}} = \text{argmin}_{\underline{\mathbf{a}}} \mathcal{L}^{\text{a}}(\underline{\mathbf{a}}) \quad \text{and} \quad \underline{\boldsymbol{\alpha}}^{\text{opt}} = \text{argmin}_{\underline{\boldsymbol{\alpha}}} \mathcal{L}^{\alpha}(\underline{\mathbf{a}}^{\text{opt}}, \underline{\boldsymbol{\alpha}}), \quad (55)$$

are solved sequentially for each ellipsoid and the results are assembled to the matrices  $\underline{\mathbf{a}}$  and  $\underline{\boldsymbol{\alpha}}$ . The loss functions are chosen as

$$\mathcal{L}^{\text{a}}(\underline{\mathbf{a}}) = \frac{1}{2} \left[ \left( \frac{\mathcal{W}_0^{0,0}(\underline{\mathbf{a}})}{\mathcal{W}_0^{0,0\text{des}}} - 1 \right)^2 + \left( \frac{\mathcal{W}_1^{0,0}(\underline{\mathbf{a}})}{\mathcal{W}_1^{0,0\text{des}}} - 1 \right)^2 + \left( \frac{\mathcal{W}_2^{0,0}(\underline{\mathbf{a}})}{\mathcal{W}_2^{0,0\text{des}}} - 1 \right)^2 \right] \quad (56)$$

and

$$\mathcal{L}^{\alpha}(\underline{\mathbf{a}}, \underline{\boldsymbol{\alpha}}) = \frac{1}{2} \cdot \text{tr} \left[ \left( \frac{\mathcal{W}_1^{0,2}(\underline{\mathbf{a}}, \underline{\boldsymbol{\alpha}})}{\mathcal{W}_1^{0,0}(\underline{\mathbf{a}})} - \frac{\mathcal{W}_1^{0,2\text{des}}}{\mathcal{W}_1^{0,0\text{des}}} \right)^2 + \left( \frac{\mathcal{W}_2^{0,2}(\underline{\mathbf{a}}, \underline{\boldsymbol{\alpha}})}{\mathcal{W}_2^{0,0}(\underline{\mathbf{a}})} - \frac{\mathcal{W}_2^{0,2\text{des}}}{\mathcal{W}_2^{0,0\text{des}}} \right)^2 \right], \quad (57)$$

where  $(\bullet)^2$  denotes an element-wise square when applied to a tensorial quantity. The optimization problems are solved using the gradient-based BFGS optimizer [85]. This stable and fast approach enables a solution in the order of milliseconds, even on a conventional laptop.

As an alternative to the presented sampling procedure, one feasible approach lies in defining a microstructure descriptor based on kernel density estimates (KDEs) of the Minkowski functionals over all ellipsoids. Such a descriptor might be used for optimization instead of sampling. Naturally, considering only KDEs of individual components neglects their correlations. A simple example shows that this behavior is not desirable: Consider an RVE with spherical

inclusions of varying size. Because the first two scalar Minkowski functionals  $\mathcal{W}_0^{0,0}$  and  $\mathcal{W}_1^{0,0}$  can be identified as the inclusion volume and surface area, respectively, reconstructing uncorrelated KDEs might lead to inclusions with low volume and high surface area, which can only be realized by flat or elongated ellipsoids. This limitation is discussed further in subsection 3.3. As a solution to this problem, adding the covariance matrix to the descriptor or considering multi-dimensional KDEs might solve this problem. However, these investigations exceed the scope of this work.

### 2.4.2. Inclusion placing

After a representative set of inclusions, i.e., ellipsoid shapes and orientations, has been reconstructed from the Minkowski tensors, a volume element is created by placing these inclusions according to  $S_2$ . This is expressed as a final optimization problem

$$\underline{\underline{p}}^{\text{opt}} = \underset{\underline{\underline{p}}}{\operatorname{argmin}} \left[ \mathcal{L}^{\text{P}}(\underline{\underline{a}}^{\text{opt}}, \underline{\underline{\alpha}}^{\text{opt}}, \underline{\underline{p}}) + \lambda \cdot \mathcal{L}^{\text{C}}(\underline{\underline{a}}^{\text{opt}}, \underline{\underline{\alpha}}^{\text{opt}}, \underline{\underline{p}}) \right] \quad (58)$$

with a descriptor loss

$$\mathcal{L}^{\text{P}}(\underline{\underline{a}}, \underline{\underline{\alpha}}, \underline{\underline{p}}) = \sum_{\mathbf{r}} \left[ \left( \tilde{S}_2^{\text{RVE,e}}(\mathbf{r}, \underline{\underline{a}}, \underline{\underline{\alpha}}, \underline{\underline{p}}) - \tilde{S}_2^{\text{des}}(\mathbf{r}) \right)^2 \right] \quad (59)$$

formulated as a sum of squared errors in the spatial correlations and a contact penalty

$$\mathcal{L}^{\text{C}}(\underline{\underline{a}}^{\text{opt}}, \underline{\underline{\alpha}}^{\text{opt}}, \underline{\underline{p}}) = \sum_{i=1}^{N^{\text{incl}}} \sum_{j=1}^{i-1} \left( \frac{\langle \delta^{\text{thr}} - \delta(i, j) \rangle}{\min \underline{\underline{a}}^{\text{opt}}} \right)^3. \quad (60)$$

Herein,  $\langle \bullet \rangle$  denotes the Macauley brackets, also known as ReLU function. Furthermore,  $\delta(i, j)$  denotes the distance<sup>3</sup> between both ellipsoids, which is penalized if it exceeds the threshold  $\delta^{\text{thr}}$ . In this work,  $\delta^{\text{thr}} = 0.1 \cdot \min \underline{\underline{a}}^{\text{opt}}$  is chosen.

Solving Equation 58 is the most computationally demanding part of the reconstruction process. Unfortunately, simple convex minimization is observed to yield suboptimal local minima. For this reason, a global optimization algorithm called Multi-Level Single-Linkage [58, 59, 36] from the *NLOpt* library [30] is used, where the low-storage variant of the gradient-based BFGS algorithm [85] serves as a local optimizer. To provide a good initialization, ellipsoids are first placed individually in order of descending inclusion volume. Without loss of generality, the largest inclusion placed at the center.

## 3. Implementation and Results

The presented method is implemented in Julia and all numerical experiments are performed on a conventional laptop and only on a single thread. It should be noted that the global optimization algorithm used in the ellipsoid placing step, which is the computational bottleneck of the method, in principle allows for straightforward parallelism. Hence, significant efficiency gains are still achievable without changing the presented formulation merely by means of coding<sup>4</sup>.

In the remainder of this section, the method is validated and tested by means of various numerical experiments. First, the reconstructed volume is set equally large as the original structure in order to validate the reconstruction and placement of spheres and ellipsoids in subsection 3.1. In these cases, the algorithm is expected to exactly recover the original structure. In contrast, this is not possible if the original structure is larger than the reconstructed domain. Such cases are investigated in subsection 3.2. Finally, the scalability and limitations of the method are discussed in subsection 3.3.

### 3.1. Validation by same-size microstructures

As a first validation, the original and reconstructed microstructure are set to an equal and small size. As shown in Figure 2, the validation structures are composed of three spherical and ellipsoidal inclusions, respectively.

<sup>3</sup>The distance is defined as the distance between the ellipsoid surfaces, not the centers. It is negative if the ellipsoids overlap and positive otherwise. Details on the distance computation are given by Perram et al. [51].

<sup>4</sup>These measures, however, do not affect the scalability of the method, but only reduce the wallclock time by a constant factor.

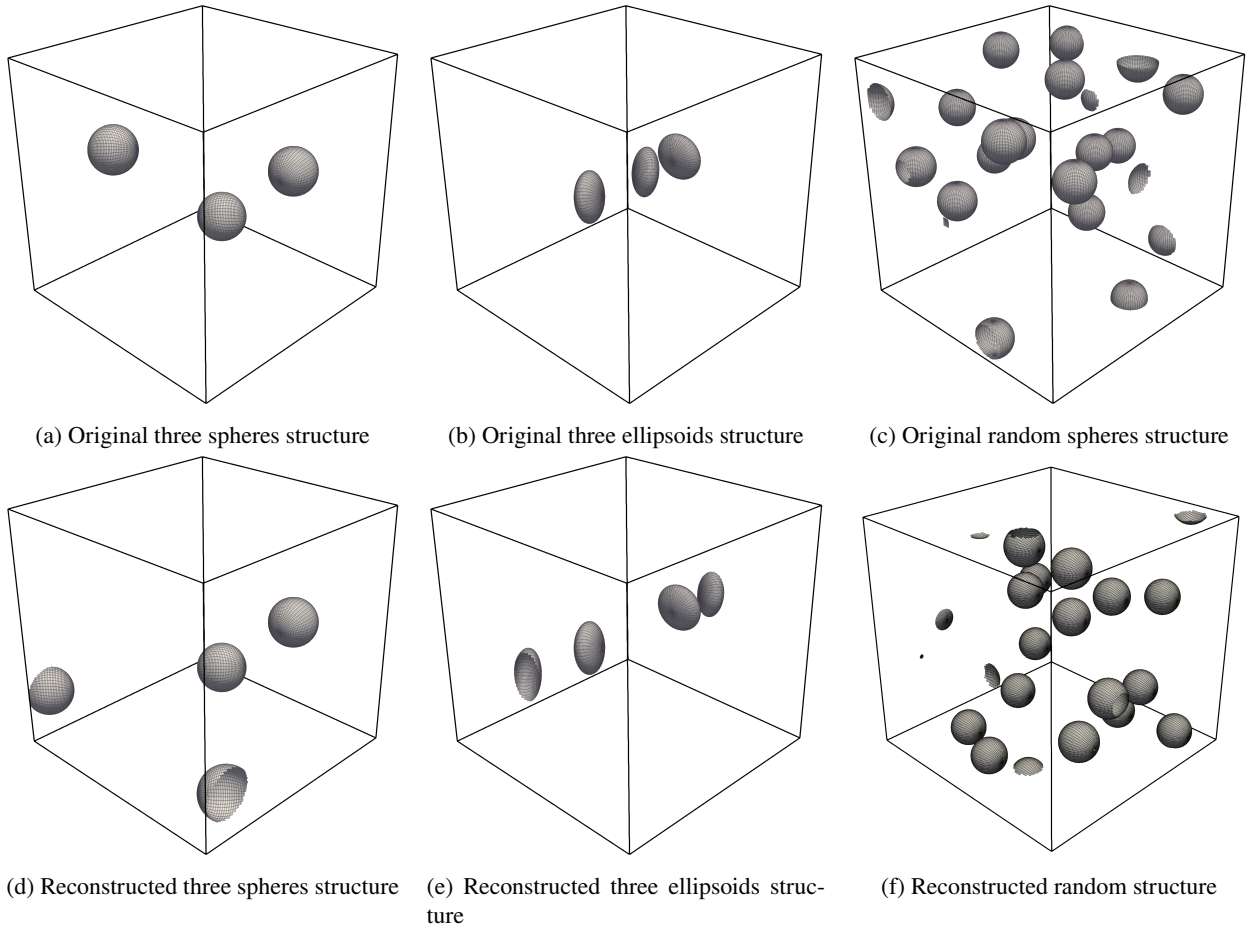


**Figure 2:** Three validation cases for same-size reconstruction. The original (top) and reconstructed (bottom) structures are identical up to point symmetry and translation for volume elements with few inclusions (left and center). This is not the case with many inclusions (right) because of local minima.

For the first structure shown in Figure 2 (a), it can be seen that the two right-hand side inclusions in the reconstruction result in Figure 2 (d) are at the exact same positions as in the original structure. At a first glance, the position of the left-hand side inclusion seems incorrect, however, it is placed at a symmetrically equivalent position. More precisely, a point symmetry around the center between the other two ellipsoids moves the inclusion out of the unit cell and under periodic boundary conditions, it re-enters at the observed position. Similarly, for the second structure in Figure 2 (b), the reconstruction in Figure 2 (e) is exact up to a point symmetry around the origin and a displacement. Because the correlations are intentionally designed to be symmetrical with respect to translation and rotation by  $180^\circ$ , it can be said that the structures are reconstructed perfectly. This is confirmed by the corresponding descriptor errors, which are given together with the performance data in Table 1. However, it should be noted that for more inclusions as in Figure 2 (c), the result (f) is acceptable but not identical to the reference, as can be seen in terms of the loss in Table 1. This is further discussed in subsection 3.3.

### 3.2. Application to reduced-size microstructures

With the method being validated for structures with a small number of inclusions, it is now applied to its intended use-case. A small and representative periodic structure is reconstructed from a larger domain, which might be a computed tomography scan in real application<sup>5</sup>. The reconstructed structure is half as large in each direction, i.e., has

<sup>5</sup>In that case, *Karambola* [33] and *MCRpy* [74] can be used to compute the desired value of the Minkowski functionals and the two-point correlation, respectively.

**Table 1**

Loss function and wallclock time for all reconstructions carried out in the present work. The wallclock time is almost identical to the duration of the inclusion placement, since the computational cost of the other steps in algorithm 1 can be neglected in practice.

ID	Reconstructed from	Size	Visualized in	$\mathcal{L}^p$	Time in s
1	three spheres	same	Figure 2 (d)	$7.3 \cdot 10^{-31}$	19.5
2	three ellipsoids	same	Figure 2 (e)	$6.5 \cdot 10^{-31}$	99.3
3	random	same	Figure 2 (f)	$1.7 \cdot 10^{-1}$	195.4
4	random	reduced	Figure 3 (d)	$2.5 \cdot 10^1$	35.1
5	pairwise inclusion	reduced	Figure 3 (e)	$8.5 \cdot 10^0$	18.7
6	chain	reduced	Figure 3 (f)	$1.1 \cdot 10^1$	196.9

an eighth of the volume. The structures are depicted in Figure 3 and the corresponding loss values and performance data are given in Table 1.

As a first example, 16 spheres of equal size are placed randomly in a volume as shown in Figure 3 (a)<sup>6</sup>. Because the original volume is eight times larger than the reconstructed structure, observing two inclusions in Figure 3 (d) meets the expectations. This is not the case if a domain is randomly sub-sampled from Figure 3 (a), which would contain between one and three inclusions.

As a second example, in order to verify the plausibility of the placement, Figure 3 (b) comprises pairs of inclusions where the relative displacement  $\mathbf{r}$  between the centers is drawn at random from uniform distributions  $\mathcal{U}$  with  $r_1 \sim U(0.15, 0.25)$ ,  $r_2 \sim U(-0.25, -0.15)$  and  $r_3 \sim U(0.19, 0.39)$ . For the reconstructed structure,  $\mathbf{r} = [0.220, -0.230, 0.311]$  is observed. Although the elements of  $\mathbf{r}$  lie within the boundaries of the uniform distributions, it is interesting to note that  $\mathbf{r}$  is neither the mean of the distributions, nor of the sampled values<sup>7</sup>.

As a third example, Figure 3 (c) comprises multiple chains of ellipsoidal inclusions with varying shape and orientation. Reconstructing inclusions chains is relevant in the context of pre-structured magnetorheological elastomers, where they are created by applying an external magnetic field during solidification. The metallic inclusions allow for switching their macroscopic behavior by applying an external magnetic field. This property enables applications to various engineering problems such as actuators and sensors [77, 79] or dampers [12, 41]. As expected, a chain is reconstructed that may be used for efficient simulations with a small domain and periodic boundary conditions. Thus, while extensive research has been conducted on the modeling and simulation [11, 32, 45, 46, 57] as well as experimental and design aspects [4, 17, 42] of MREs, a tailored reconstruction algorithm may enable a stronger interaction between these fields to bring MREs closer to practical application.

### 3.3. Scalability and limitations

Because the degrees of freedom of the inclusions are considered directly instead of discretizing them to a voxel grid or tessellating the surface, the dimensionality of the optimization problem is independent of the volume size or resolution, but rather grows linearly with the number of inclusions. The cost of reconstructing ellipsoid shapes and orientations from Minkowski tensor distributions scales linearly in the number of inclusions and can be neglected when compared to the inclusion placement. In this context, the computational cost of evaluating the loss function scales as the spatial correlations and the surface-to-surface distance computation. In the current implementation, distances are computed between all ellipsoids, making this term scale as  $\mathcal{O}((N^{\text{incl}})^2)$ , but a verlet list or a similar data structure could be used to reduce this number. The distance computation cannot be discarded to save computational effort, because avoiding collisions is not only a physical requirement in the materials of interest, but also a mathematical requirement for the validity of the presented analytical solutions. In order to compute the Fourier coefficients of the indicator function,  $\mathcal{O}(\overline{N}_1 \overline{N}_2 \overline{N}_3)$  coefficients need to be computed for each of the  $N^{\text{incl}}$  ellipsoids. The Fourier transform in Equation 51 to obtain  $\tilde{\mathcal{S}}_2^{\text{RVE,e}}$  from  $|\overline{\mathcal{I}}_{jkl}^{\text{RVE,e}}|^2$  scales as  $\mathcal{O}(\overline{N}_1 \overline{N}_2 \overline{N}_3 \log \overline{N}_1 \log \overline{N}_2 \log \overline{N}_3)$ . In principle, one might equally well use  $|\overline{\mathcal{I}}_{jkl}^{\text{RVE,e}}|^2$  as a descriptor in the placement loss function Equation 59 to save computational effort in future works. However, the computational cost of evaluating the loss function does not provide a good estimate

<sup>6</sup>This is identical to Figure 2 (c).

<sup>7</sup>Not shown here.

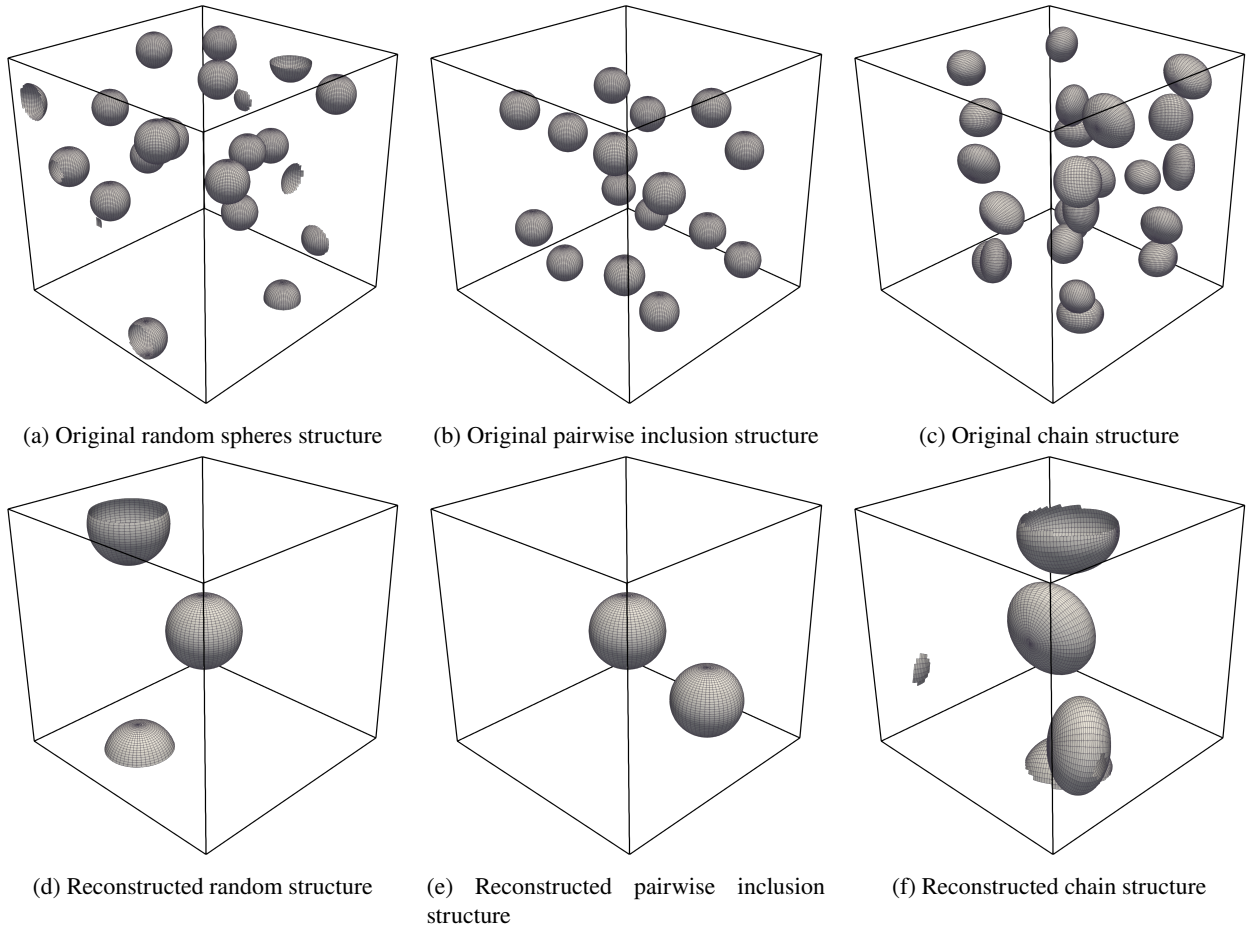


**Figure 3:** Three validation cases for reduced-size reconstruction, i.e. where the reconstruction aims at generating a small, periodic volume element (bottom) from a larger structure (top). The size of the reconstructed volume elements is magnified by a factor of two per direction for visualization purposes. It can be seen that the main characteristics of the original structure are captured well.

for actually solving the optimization problem in practice because local minima become more pronounced as  $N^{\text{incl}}$  increases and significantly more iterations are needed. In fact, while efficiently reconstructing a small volume element from a larger reference with inclusion chains as in Figure 3 (c) is a strength of the method, an equally large volume element cannot be reconstructed at all in a feasible time because of local minima. Hence, if this is of interest, a suitable or even tailored optimizer is required or the formulation of the optimization problem needs to be adapted.

A second limitation naturally lies in the shape of the inclusions, which is approximated as ellipsoidal in this work. If the considered inclusions significantly differ, such as the spiral in Figure 4 (a), it should be noted that they are not approximated in terms of spatial extent, but in terms of Minkowski functionals. Since the first two scalar Minkowski functionals coincide with the volume fraction and the surface area of the inclusion, non-convex inclusions can only be approximated by very flat ellipsoids. Based on this observation, the orientation and the exact aspect ratios are determined by the remaining functionals and the reader is referred to [69] for an interpretation of the same. The closest possible ellipsoid to Figure 4 (a) in terms of Minkowski functionals is shown in Figure 4 (b) and demonstrates that Figure 4 (a) clearly exceeds the range of applicability of the method. Although complex inclusions can be approximated very well by overlapping simple geometric shapes such as spheres in [47], this would later need to be considered in deriving global descriptors such as the two-point correlation. As an alternative solution, other inclusion shape descriptors might be considered, such as the cluster correlation function [29]. It can be derived analytically based





**Figure 4:** Investigation of the reconstruction of strongly non-ellipsoidal inclusions. Because Minkowski functionals are used for the reconstruction, the approximation of the shape in (a) is not optimized in terms of the spatial extent, but rather in terms of volume, surface area and other captures characteristics.

on the presented results by replacing  $\bar{I}_{jkl}^{\text{RVE,e}}$  in Equation 51 by  $\bar{I}_{jkl}^{\text{ellipsoid}}$ . This is left for future investigations since strongly non-ellipsoidal inclusions lie beyond the scope of this work.

In summary, while the method is highly effective and accurate for reconstructing a small number of ellipsoidal inclusions, further developments are needed for cases where these inclusions are not actually ellipsoidal or are very numerous.

#### 4. Conclusions

In this work, a tailored reconstruction algorithm is presented for microstructures with ellipsoidal inclusions like magnetorheological elastomers. Unlike in previous work, these inclusions are non-overlapping. Building upon gradient-based microstructure reconstruction as in *MCRpy* [74] and inspired by the low-dimensional microstructure approximation in the work of Scheunemann et al. [65, 64], a high efficiency is reached. This is rooted in four main features of the method, namely (i) the low dimensionality of the minimization problem, (ii) the subdivision of the optimization into consecutive stages, (iii) the computational efficiency of the derived analytical solutions for the descriptors and (iv) the differentiability of the same, allowing for gradient-based optimization.

For this, analytical expressions are derived to compute the Minkowski functionals and the spatial two-point correlation<sup>8</sup> as a function of the microstructure parametrization, i.e. the ellipsoid semiaxes, orientations and positions. Based on these descriptors, an algorithm is presented that sequentially samples individual tuples of Minkowski functionals, recovers the corresponding inclusion shapes and orientations and finally places all ellipsoids in the volume element. This method is validated by means of various numerical experiments. It is concluded that the method is very well suited for efficiently generating small statistical volume elements from larger structures, however, a transparent summary of the method's limitations is also given in the following.

By directly representing inclusions analytically, the computational cost of the method is independent of the structure resolution, however, it does scale with the number of inclusions. Although the cost function for determining the ellipsoid location can still be evaluated efficiently for ten or more inclusions, the optimization problem itself scales very unfavorably, as the increasing number of local minima overstrains the utilized global optimizer. Besides that, although analytically deriving descriptors as functions of the microstructure parametrization yields remarkable efficiency, this derivation can also represent a hurdle when new descriptors are to be used<sup>9</sup>. Finally, it is observed that the nature of the Minkowski functionals leads to unexpected behaviour if the inclusions to reconstruct are strongly non-ellipsoidal.

For future work, besides the derivation of further descriptors, it should also be investigated how well the limit case of elongated ellipsoids can be used to approximate short fibers or if the descriptor derivations would need to

<sup>8</sup>Although not used, the cluster correlation function can be obtained trivially from this derivation.

<sup>9</sup>Note in this context the ambiguity of the two-point correlation function [21] and the comparatively low effort of adding descriptors to *MCRpy* [74].

be repeated for a different geometry. Furthermore, it would be promising to develop a microstructure descriptor to quantify the distribution of Minkowski functionals instead of individual inclusions. As discussed previously, this could be achieved by a kernel density estimate. Finally, reconstructing 3D structures from 2D slices would enable a plethora of applications. However, such an extension cannot be performed as easily as in voxel- and slice-based methods [83, 35, 73] because 3D descriptors need to be corrected for the fact that inclusions are cut at random [2].

## Acknowledgements

The group of M. Kästner thanks the German Research Foundation DFG which supported this work under Grant number KA 3309/18-1. The authors are grateful to the Centre for Information Services and High Performance Computing [Zentrum für Informationsdienste und Hochleistungsrechnen (ZIH)] TU Dresden for providing its facilities for high throughput calculations.

## Competing interest statement

The authors declare no competing interest.

## Data availability statement

The code and data is made available by the authors upon reasonable request.

## CRedit authorship contribution statement

**Paul Seibert:** Conceptualization, Data Curation, Formal Analysis, Investigation, Methodology, Supervision, Validation, Visualization, Writing - original draft, Writing - review and editing. **Markus Husert:** Investigation, Data Curation, Formal Analysis, Investigation, Methodology, Software, Validation, Visualization, Writing - original draft, Writing - review and editing. **Maximilian P. Wollner:** Conceptualization, Formal Analysis, Investigation, Methodology, Software, Supervision, Writing - review and editing. **Karl A. Kalina:** Conceptualization, Methodology, Supervision, Writing - original draft, Writing - review and editing. **Markus Kästner:** Conceptualization, Funding acquisition, Resources, Writing - review and editing.

## A. Derivation of analytical expressions for Minkowski functionals

In order to calculate analytical expressions for Minkowski functionals of ellipsoids, the expressions of the surface element  $dS$ , the unit normal vector  $\mathbf{n}$  and the mean curvature  $H$  are derived in the following. The covariant basis vectors are defined as

$$\mathbf{g}_\varphi = \frac{\partial \mathbf{x}}{\partial \varphi} = -a_1 \sin(\theta) \sin(\varphi) \mathbf{e}_1 + a_2 \sin(\theta) \cos(\varphi) \mathbf{e}_2 \quad \text{and} \quad (61)$$

$$\mathbf{g}_\theta = \frac{\partial \mathbf{x}}{\partial \theta} = a_1 \cos(\theta) \cos(\varphi) \mathbf{e}_1 + a_2 \cos(\theta) \sin(\varphi) \mathbf{e}_2 - a_3 \sin(\theta) \mathbf{e}_3. \quad (62)$$

and allow computing a surface element  $dS$  of the ellipsoid surface [13] as

$$dS = \sqrt{EG - F^2} d\theta d\varphi. \quad (63)$$

using the coefficients

$$E = \mathbf{g}_\varphi \cdot \mathbf{g}_\varphi = \sin^2(\theta) [(a_1)^2 \sin^2(\varphi) + (a_2)^2 \cos^2(\varphi)], \quad (64)$$

$$F = \mathbf{g}_\theta \cdot \mathbf{g}_\varphi = [(a_2)^2 - (a_1)^2] \cos(\theta) \sin(\theta) \cos(\varphi) \sin(\varphi) \quad \text{and} \quad (65)$$

$$G = \mathbf{g}_\theta \cdot \mathbf{g}_\theta = \cos^2(\theta) [(a_1)^2 \cos^2(\varphi) + (a_2)^2 \sin^2(\varphi)] + (a_3)^2 \sin^2(\theta). \quad (66)$$

The unit normal vector  $\mathbf{n}$  on the ellipsoid surface is defined as

$$\mathbf{n} = \frac{\mathbf{g}_\varphi \times \mathbf{g}_\theta}{|\mathbf{g}_\varphi \times \mathbf{g}_\theta|}, \quad (67)$$

where the cross product of the covariant basis vectors is

$$\mathbf{g}_\varphi \times \mathbf{g}_\theta = -a_2 a_3 \sin^2(\theta) \cos(\varphi) \mathbf{e}_1 - a_1 a_3 \sin^2(\theta) \sin(\varphi) \mathbf{e}_2 - a_1 a_2 \sin(\theta) \cos(\theta) \mathbf{e}_3 \quad (68)$$

with the Euclidean norm

$$\left| \mathbf{g}_\varphi \times \mathbf{g}_\theta \right| = \sin(\theta) \sqrt{(a_2)^2 (a_3)^2 \sin^2(\theta) \cos^2(\varphi) + (a_1)^2 (a_3)^2 \sin^2(\theta) \sin^2(\varphi) + (a_1)^2 (a_2)^2 \cos^2(\theta)} \quad (69)$$

$$= \sin(\theta) \sqrt{\sin^2(\varphi) f_1(\theta) + \cos^2(\varphi) f_2(\theta)} = \sqrt{EG - F^2}, \quad (70)$$

and the auxiliary functions

$$f_1(\theta) = (a_1)^2 [(a_3)^2 \sin^2(\theta) + (a_2)^2 \cos^2(\theta)] \quad \text{and} \quad (71)$$

$$f_2(\theta) = (a_2)^2 [(a_3)^2 \sin^2(\theta) + (a_1)^2 \cos^2(\theta)]. \quad (72)$$

Substituting Equation 68 and Equation 69 into Equation 67 yields the required expression for the unit normal vector

$$\mathbf{n} = n_1 \mathbf{e}_1 + n_2 \mathbf{e}_2 + n_3 \mathbf{e}_3 \quad (73)$$

$$= \frac{1}{\sqrt{EG - F^2}} (-a_2 a_3 \sin^2(\theta) \cos(\varphi) \mathbf{e}_1 - a_1 a_3 \sin^2(\theta) \sin(\varphi) \mathbf{e}_2 - a_1 a_2 \sin(\theta) \cos(\theta) \mathbf{e}_3). \quad (74)$$

The derivatives of the covariant basis vectors with regards to the coordinates  $\theta$  and  $\varphi$

$$\mathbf{g}_{\varphi,\varphi} = \frac{\partial \mathbf{g}_\varphi}{\partial \varphi} = -a_1 \sin(\theta) \cos(\varphi) \mathbf{e}_1 - a_2 \sin(\theta) \sin(\varphi) \mathbf{e}_2, \quad (75)$$

$$\mathbf{g}_{\theta,\varphi} = \mathbf{g}_{\varphi,\theta} = \frac{\partial \mathbf{g}_\theta}{\partial \varphi} = \frac{\partial \mathbf{g}_\varphi}{\partial \theta} = -a_1 \cos(\theta) \sin(\varphi) \mathbf{e}_1 + a_2 \cos(\theta) \cos(\varphi) \mathbf{e}_2 \quad \text{and} \quad (76)$$

$$\mathbf{g}_{\theta,\theta} = \frac{\partial \mathbf{g}_\theta}{\partial \theta} = -a_1 \sin(\theta) \cos(\varphi) \mathbf{e}_1 - a_2 \sin(\theta) \sin(\varphi) \mathbf{e}_2 - a_3 \cos(\theta) \mathbf{e}_3 \quad (77)$$

define the coefficients of the second fundamental form of differential geometry

$$e = \mathbf{n} \cdot \mathbf{g}_{\varphi,\varphi} = \frac{a_1 a_2 a_3 \sin^3(\theta)}{\sqrt{EG - F^2}}, \quad (78)$$

$$f = \mathbf{n} \cdot \mathbf{g}_{\theta,\varphi} = 0 \quad \text{and} \quad (79)$$

$$g = \mathbf{n} \cdot \mathbf{g}_{\theta,\theta} = \frac{a_1 a_2 a_3 \sin(\theta)}{\sqrt{EG - F^2}}, \quad (80)$$

which can be used to compute the mean curvature  $H$  as

$$H = \frac{1}{2}(\kappa_1 + \kappa_2) = \frac{1}{2} \frac{eG - 2fF + gE}{EG - F^2} = \frac{a_1 a_2 a_3}{2} \frac{f_3(\theta) \sin^2(\varphi) + f_4(\theta) \cos^2(\varphi)}{[f_1(\theta) \sin^2(\varphi) + f_2(\theta) \cos^2(\varphi)]^{\frac{3}{2}}}, \quad (81)$$

with the auxiliary functions

$$f_3(\theta) = [(a_1)^2 + (a_3)^2] \sin^2(\theta) + [(a_1)^2 + (a_2)^2] \cos^2(\theta) \quad \text{and} \quad (82)$$

$$f_4(\theta) = [(a_2)^2 + (a_3)^2] \sin^2(\theta) + [(a_1)^2 + (a_2)^2] \cos^2(\theta). \quad (83)$$

With the definition of the ellipsoid surface in Equation 27, the surface element in Equation 63, the normal vector in Equation 74 and the mean curvature in Equation 81, the tensorial Minkowski functionals of an ellipsoid can be calculated.

## References

- [1] Adam, A., Wang, F., Li, X., 2022. Efficient reconstruction and validation of heterogeneous microstructures for energy applications. *International Journal of Energy Research*, er.8578 URL: <https://onlinelibrary.wiley.com/doi/10.1002/er.8578>, doi:10.1002/er.8578.
- [2] Anderson, M.J., Basoalto, H.C., 2023. Automated Stereology and Uncertainty Quantification Considering Spherical Non-Penetrating Dispersions. *Crystals* 13, 464. URL: <https://www.mdpi.com/2073-4352/13/3/464>, doi:10.3390/cryst13030464.
- [3] Bargmann, S., Klusemann, B., Markmann, J., Schnabel, J.E., Schneider, K., Soyarslan, C., Wilmers, J., 2018. Generation of 3D representative volume elements for heterogeneous materials: A review. *Progress in Materials Science* 96, 322–384. URL: <https://linkinghub.elsevier.com/retrieve/pii/S0079642518300161>, doi:10.1016/j.pmatsci.2018.02.003.
- [4] Bastola, A.K., Hossain, M., 2020. A Review on Magneto-Mechanical Characterizations of Magnetorheological Elastomers. *Composites Part B: Engineering* 200, 108348. doi:10.1016/j.compositesb.2020.108348.
- [5] Beisbart, C., Dahlke, R., Mecke, K., Wagner, H., 2002. Vector- and Tensor-Valued Descriptors for Spatial Patterns, in: Mecke, K., Stoyan, D. (Eds.), *Morphology of Condensed Matter: Physics and Geometry of Spatially Complex Systems*. Springer, Berlin, Heidelberg. *Lecture Notes in Physics*, pp. 238–260. URL: [https://doi.org/10.1007/3-540-45782-8\\_10](https://doi.org/10.1007/3-540-45782-8_10), doi:10.1007/3-540-45782-8\_10.
- [6] Bergström, J.S., Boyce, M.C., 1999. Mechanical Behavior of Particle Filled Elastomers. *Rubber Chemistry and Technology* 72, 633–656. URL: <https://meridian.allenpress.com/rct/article/72/4/633/92838/Mechanical-Behavior-of-Particle-Filled-Elastomers>, doi:10.5254/1.3538823.
- [7] Bhaduri, A., Gupta, A., Olivier, A., Graham-Brady, L., 2021. An efficient optimization based microstructure reconstruction approach with multiple loss functions. *Computational Materials Science* 199, 110709. URL: <https://www.sciencedirect.com/science/article/pii/S0927025621004365>, doi:10.1016/j.commatsci.2021.110709.
- [8] Bostanabad, R., 2020. Reconstruction of 3D Microstructures from 2D Images via Transfer Learning. *Computer-Aided Design* 128, 102906. doi:10.1016/j.cad.2020.102906.
- [9] Bostanabad, R., Chen, W., Apley, D., 2016. Characterization and reconstruction of 3D stochastic microstructures via supervised learning. *Journal of Microscopy* 264, 282–297. doi:10.1111/jmi.12441.
- [10] Bostanabad, R., Zhang, Y., Li, X., Kearney, T., Brinson, L.C., Apley, D.W., Liu, W.K., Chen, W., 2018. Computational microstructure characterization and reconstruction: Review of the state-of-the-art techniques. *Progress in Materials Science* 95, 1–41. doi:10.1016/j.pmatsci.2018.01.005.
- [11] Bustamante, R., Dorfmann, A., Ogden, R.W., 2011. Numerical Solution of Finite Geometry Boundary-Value Problems in Nonlinear Magnetoelasticity. *International Journal of Solids and Structures* 48, 874–883. doi:10.1016/j.ijsolstr.2010.11.021.
- [12] Carlson, J.D., Jolly, M.R., 2000. MR Fluid, Foam and Elastomer Devices. *Mechatronics* 10, 555–569. doi:[http://dx.doi.org/10.1016/S0957-4158\(99\)00064-1](http://dx.doi.org/10.1016/S0957-4158(99)00064-1).
- [13] Carmo, M.P.d., 2016. *Differential Geometry of Curves and Surfaces: Revised and Updated Second Edition*. Courier Dover Publications. Google-Books-ID: gg2xDQAAQBAJ.
- [14] Chen, J., Liu, J., Peng, Z., Yao, Y., Chen, S., 2021. The microscopic mechanism of size effect in silica-particle reinforced silicone rubber composites. *Engineering Fracture Mechanics* 255, 107945. URL: <https://www.sciencedirect.com/science/article/pii/S0013794421003714>, doi:10.1016/j.engfracmech.2021.107945.
- [15] Chen, W., Iyer, A., Bostanabad, R., 2022. Data-centric design of microstructural materials systems. *Engineering*, S209580992200056X URL: <https://linkinghub.elsevier.com/retrieve/pii/S209580992200056X>, doi:10.1016/j.eng.2021.05.022.
- [16] Choi, J.B., Nguyen, P.C.H., Sen, O., Udaykumar, H.S., Baek, S., 2022. Artificial intelligence approaches for materials-by-design of energetic materials: state-of-the-art, challenges, and future directions, 23.
- [17] Danas, K., Kankanala, S., Triantafyllidis, N., 2012. Experiments and Modeling of Iron-Particle-Filled Magnetorheological Elastomers. *Journal of the Mechanics and Physics of Solids* 60, 120–138. doi:10.1016/j.jmps.2011.09.006.
- [18] Dürerth, C., Seibert, P., Rücker, D., Handford, S., Kästner, M., Gude, M., 2023. Conditional diffusion-based microstructure reconstruction. *Materials Today Communications*, 105608 URL: <https://www.sciencedirect.com/science/article/pii/S2352492823002982>, doi:10.1016/j.mtcomm.2023.105608.
- [19] Eruşlu, S.O., 2021. Finite element modeling of glass particle reinforced epoxy composites under uniaxial compression and sliding wear. *Materials Testing* 63, 645–653. URL: <https://www.degruyter.com/document/doi/10.1515/mt-2020-0106/html>, doi:10.1515/mt-2020-0106.
- [20] Eshelby, J.D., 1959. The Elastic Field Outside an Ellipsoidal Inclusion. *Proceedings of the Royal Society of London. Series A, Mathematical and Physical Sciences* 252, 561–569. URL: <http://www.jstor.org/stable/100791>.
- [21] Fernández, M., Fritzen, F., 2020. On the generation of periodic discrete structures with identical two-point correlation. *arXiv:2002.01234 [cs]*, 1–30 arXiv: 2002.01234.
- [22] Fokina, D., Muravleva, E., Ovchinnikov, G., Oseledets, I., 2020. Microstructure synthesis using style-based generative adversarial networks. *Physical Review E* 101, 1–13. doi:10.1103/PhysRevE.101.043308.
- [23] Fu, J., Wang, M., Xiao, D., Zhong, S., Ge, X., Wu, M., Evans, B., 2023. Hierarchical reconstruction of 3D well-connected porous media from 2D exemplars using statistics-informed neural network. *Computer Methods in Applied Mechanics and Engineering* 410, 116049. URL: <https://linkinghub.elsevier.com/retrieve/pii/S0045782523001731>, doi:10.1016/j.cma.2023.116049.
- [24] Gerke, K.M., Karsanina, M.V., 2015. Improving stochastic reconstructions by weighting correlation functions in an objective function. *EPL (Europhysics Letters)* 111, 56002. URL: <https://iopscience.iop.org/article/10.1209/0295-5075/111/56002>, doi:10.1209/0295-5075/111/56002.
- [25] Groeber, M.A., Jackson, M.A., 2014. DREAM.3D: A Digital Representation Environment for the Analysis of Microstructure in 3D. *Integrating Materials and Manufacturing Innovation* 3, 56–72. doi:10.1186/2193-9772-3-5.

- [26] Henkes, A., Wessels, H., 2022. Three-dimensional microstructure generation using generative adversarial neural networks in the context of continuum micromechanics. *Computer Methods in Applied Mechanics and Engineering* 400, 115497. URL: <https://linkinghub.elsevier.com/retrieve/pii/S0045782522005126>, doi:10.1016/j.cma.2022.115497.
- [27] Hiptmair, F., Major, Z., Haßlacher, R., Hild, S., 2015. Design and Application of Permanent Magnet Flux Sources for Mechanical Testing of Magnetoactive Elastomers at Variable Field Directions. *Review of Scientific Instruments* 86, 085107. doi:10.1063/1.4927714. publisher: AIP Publishing.
- [28] Horny, D., Schulz, K., 2022. Analysis of interpenetrating metal ceramic composite structures using an enhanced random sequential absorption microstructure generation algorithm. *Journal of Materials Science* 57, 8869–8889. URL: <https://link.springer.com/10.1007/s10853-022-07180-1>, doi:10.1007/s10853-022-07180-1.
- [29] Jiao, Y., Stillinger, F.H., Torquato, S., 2009. A superior descriptor of random textures and its predictive capacity. *Proceedings of the National Academy of Sciences* 106, 17634–17639. doi:10.1073/pnas.0905919106.
- [30] Johnson, S.G., 2023. The NLOpt nonlinear-optimization package. URL: <https://github.com/stevengj/nlopt>. original-date: 2013-08-27T16:59:11Z.
- [31] Kalina, K.A., Linden, L., Brummund, J., Kästner, M., 2023. FEANN: an efficient data-driven multiscale approach based on physics-constrained neural networks and automated data mining. *Computational Mechanics* URL: <https://link.springer.com/10.1007/s00466-022-02260-0>, doi:10.1007/s00466-022-02260-0.
- [32] Kalina, K.A., Raßloff, A., Wollner, M., Metsch, P., Brummund, J., Kästner, M., 2020. Multiscale modeling and simulation of magneto-active elastomers based on experimental data. *Physical Sciences Reviews* 0, 20200012. URL: <https://www.degruyter.com/document/doi/10.1515/psr-2020-0012/html>, doi:10.1515/psr-2020-0012.
- [33] Kapfer, S., Schaller, F., 2023. karambola: 3D Minkowski Tensor Package. URL: <https://github.com/morphometry/karambola>.
- [34] Karanina, M.V., Gerke, K.M., 2018. Hierarchical Optimization: Fast and Robust Multiscale Stochastic Reconstructions with Rescaled Correlation Functions. *Physical Review Letters* 121, 265501. URL: <https://link.aps.org/doi/10.1103/PhysRevLett.121.265501>, doi:10.1103/PhysRevLett.121.265501.
- [35] Kench, S., Cooper, S.J., 2021. Generating 3D structures from a 2D slice with GAN-based dimensionality expansion. *Nat Mach Intell* 3, 299–305. doi:<https://doi.org/10.1038/s42256-021-00322-1>. arXiv: 2102.07708.
- [36] Kucherenko, S., Sytsko, Y., 2005. Application of Deterministic Low-Discrepancy Sequences in Global Optimization. *Computational Optimization and Applications* 30, 297–318. URL: <http://link.springer.com/10.1007/s10589-005-4615-1>, doi:10.1007/s10589-005-4615-1.
- [37] Kuhn, J., Schneider, M., Sonnweber-Ribic, P., Böhlke, T., 2022. Generating polycrystalline microstructures with prescribed tensorial texture coefficients. *Computational Mechanics* 70, 639–659. URL: <https://link.springer.com/10.1007/s00466-022-02186-7>, doi:10.1007/s00466-022-02186-7.
- [38] Latka, K., Doskar, M., Zeman, J., 2021. Microstructure reconstruction via artificial neural networks: A combination of causal and non-causal approach. *Acta Polytechnica* , 7.
- [39] Lee, K.H., Yun, G.J., 2023. Microstructure reconstruction using diffusion-based generative models. *Mechanics of Advanced Materials and Structures* , 1–19 URL: <https://www.tandfonline.com/doi/full/10.1080/15376494.2023.2198528>, doi:10.1080/15376494.2023.2198528.
- [40] Li, X., Zhang, Y., Zhao, H., Burkhart, C., Brinson, L.C., Chen, W., 2018. A Transfer Learning Approach for Microstructure Reconstruction and Structure-property Predictions. *Scientific Reports* 8, 13461. doi:10.1038/s41598-018-31571-7.
- [41] Li, Y., Li, J., Tian, T., Li, W., 2013. A Highly Adjustable Magnetorheological Elastomer Base Isolator for Applications of Real-Time Adaptive Control. *Smart Materials and Structures* 22, 095020. doi:10.1088/0964-1726/22/9/095020.
- [42] Lokander, M., Stenberg, B., 2003. Improving the Magnetorheological Effect in Isotropic Magnetorheological Rubber Materials. *Polymer Testing* 22, 677–680. doi:10.1016/S0142-9418(02)00175-7.
- [43] Martin, J.E., Anderson, R.A., Williamson, R.L., 2003. Generating strange magnetic and dielectric interactions: Classical molecules and particle foams. *The Journal of Chemical Physics* 118, 1557–1570. URL: <https://doi.org/10.1063/1.1528892>, doi:10.1063/1.1528892.
- [44] Mehta, A., Schneider, M., 2022. A sequential addition and migration method for generating microstructures of short fibers with prescribed length distribution. *Computational Mechanics* URL: <https://link.springer.com/10.1007/s00466-022-02201-x>, doi:10.1007/s00466-022-02201-x.
- [45] Metsch, P., Schmidt, H., Sindesberger, D., Kalina, K.A., Brummund, J., Auernhammer, G.K., Monkman, G.J., Kästner, M., 2020. Field-Induced Interactions in Magneto-Active Elastomers - A Comparison of Experiments and Simulations. *Smart Materials and Structures* 29. doi:10.1088/1361-665X/ab92dc.
- [46] Mukherjee, D., Bodelot, L., Danas, K., 2019. Microstructurally-Guided Explicit Continuum Models for Isotropic Magnetorheological Elastomers with Iron Particles. *International Journal of Non-Linear Mechanics* 120, 103380. doi:10.1016/j.ijnonlinmec.2019.103380.
- [47] Nakka, R., Harursampath, D., Pathan, M., Ponnusami, S.A., 2022. A computationally efficient approach for generating RVEs of various inclusion/fibre shapes. *Composite Structures* 291, 115560. URL: <https://linkinghub.elsevier.com/retrieve/pii/S0263822322003452>, doi:10.1016/j.compstruct.2022.115560.
- [48] Niezgodna, S., Fullwood, D., Kalidindi, S., 2008. Delineation of the space of 2-point correlations in a composite material system. *Acta Materialia* 56, 5285–5292. doi:10.1016/j.actamat.2008.07.005.
- [49] Olivier, A., Giovanis, D.G., Aakash, B., Chauhan, M., Vandanapu, L., Shields, M.D., 2020. UQpy: A general purpose Python package and development environment for uncertainty quantification. *Journal of Computational Science* 47, 101204. URL: <https://linkinghub.elsevier.com/retrieve/pii/S1877750320305056>, doi:10.1016/j.jocs.2020.101204.
- [50] Pant, L.M., Mitra, S.K., Secanell, M., 2015. Multigrid hierarchical simulated annealing method for reconstructing heterogeneous media. *Physical Review E* 92, 063303. URL: <https://link.aps.org/doi/10.1103/PhysRevE.92.063303>, doi:10.1103/PhysRevE.92.063303.

- [51] Perram, J.W., Wertheim, M.S., 1985. Statistical mechanics of hard ellipsoids. I. Overlap algorithm and the contact function. *Journal of Computational Physics* 58, 409–416. URL: <https://www.sciencedirect.com/science/article/pii/0021999185901718>, doi:10.1016/0021-9991(85)90171-8.
- [52] Phan, J., Ruspini, L., Kiss, G., Lindseth, F., 2022. Size-invariant 3D generation from a single 2D rock image. *Journal of Petroleum Science and Engineering*, 9.
- [53] Piasecki, R., Olchawa, W., Frączek, D., Bartecka, A., 2020. A Two-Stage Reconstruction of Microstructures with Arbitrarily Shaped Inclusions. *Materials* 13, 2748. doi:10.3390/ma13122748.
- [54] Piasecki, R., Plastino, A., 2010. Entropic descriptor of a complex behaviour. *Physica A: Statistical Mechanics and its Applications* 389, 397–407. doi:10.1016/j.physa.2009.10.013.
- [55] Prasad, M., Vajragupta, N., Hartmaier, A., 2019. Kanapy: A Python package for generating complex synthetic polycrystalline microstructures. *Journal of Open Source Software* 4, 1732. URL: <https://joss.theoj.org/papers/10.21105/joss.01732>, doi:10.21105/joss.01732.
- [56] Quey, R., Kasemer, M., 2022. The Neper/FEPX Project: Free / Open-source Polycrystal Generation, Deformation Simulation, and Post-processing. *IOP Conference Series: Materials Science and Engineering* 1249, 012021. URL: <https://iopscience.iop.org/article/10.1088/1757-899X/1249/1/012021>, doi:10.1088/1757-899X/1249/1/012021.
- [57] Rambausek, M., Mukherjee, D., Danas, K., 2022. A Computational Framework for Magnetically Hard and Soft Viscoelastic Magnetorheological Elastomers. *Computer Methods in Applied Mechanics and Engineering* 391, 114500. doi:10.1016/j.cma.2021.114500.
- [58] Rinnooy Kan, A.H.G., Timmer, G.T., 1987a. Stochastic global optimization methods part I: Clustering methods. *Mathematical Programming* 39, 27–56. URL: <http://link.springer.com/10.1007/BF02592070>, doi:10.1007/BF02592070.
- [59] Rinnooy Kan, A.H.G., Timmer, G.T., 1987b. Stochastic global optimization methods part II: Multi level methods. *Mathematical Programming* 39, 57–78. URL: <http://link.springer.com/10.1007/BF02592071>, doi:10.1007/BF02592071.
- [60] Robertson, A.E., Kalidindi, S.R., 2021. Efficient Generation of Anisotropic N-Field Microstructures From 2-Point Statistics Using Multi-Output Gaussian Random Fields. *SSRN Electronic Journal* URL: <https://www.ssrn.com/abstract=3949516>, doi:10.2139/ssrn.3949516.
- [61] Robertson, A.E., Kelly, C., Buzzy, M., Kalidindi, S.R., 2023. Local-Global Decompositions for Conditional Microstructure Generation. preprint. *SSRN*. URL: <https://www.ssrn.com/abstract=4388214>, doi:10.2139/ssrn.4388214.
- [62] Rozman, M.G., Utz, M., 2001. Efficient reconstruction of multiphase morphologies from correlation functions. *Physical Review E* 63, 1–8. doi:10.1103/PhysRevE.63.066701.
- [63] Sahimi, M., Tahmasebi, P., 2021. Reconstruction, optimization, and design of heterogeneous materials and media: Basic principles, computational algorithms, and applications. *Physics Reports* 939, 1–82. URL: <https://linkinghub.elsevier.com/retrieve/pii/S0370157321003719>, doi:10.1016/j.physrep.2021.09.003.
- [64] Scheunemann, L., 2017. Scale-bridging of Elasto-Plastic Microstructures using Statistically Similar Representative Volume Elements. Ph.D. thesis.
- [65] Scheunemann, L., Balzani, D., Brands, D., Schröder, J., 2015. Design of 3D statistically similar Representative Volume Elements based on Minkowski functionals. *Mechanics of Materials* 90, 185–201. doi:10.1016/j.mechmat.2015.03.005.
- [66] Schneider, M., 2017. The sequential addition and migration method to generate representative volume elements for the homogenization of short fiber reinforced plastics. *Computational Mechanics* 59, 247–263. URL: <http://link.springer.com/10.1007/s00466-016-1350-7>, doi:10.1007/s00466-016-1350-7.
- [67] Schneider, R., Schuster, R., 1999. Tensor valuations on convex bodies and integral geometry. *Albert-Ludwigs-Univ., Math. Fak.*
- [68] Schröder, J., 2014. A numerical two-scale homogenization scheme: the FE2-method, in: Schröder, J., Hackl, K. (Eds.), *Plasticity and Beyond: Microstructures, Crystal-Plasticity and Phase Transitions*. Springer, Vienna. CISM International Centre for Mechanical Sciences, pp. 1–64. URL: [https://doi.org/10.1007/978-3-7091-1625-8\\_1](https://doi.org/10.1007/978-3-7091-1625-8_1), doi:10.1007/978-3-7091-1625-8\_1.
- [69] Schröder-Turk, E. G., Kapfer, S., Breidenbach, B., Beisbart, C., Mecke, K., 2010. Tensorial Minkowski functionals and anisotropy measures for planar patterns. *Journal of Microscopy* 238, 57–74. URL: <http://www3.interscience.wiley.com/journal/122659371/abstract>, doi:10.1111/j.1365-2818.2009.03331.x.
- [70] Schröder-Turk, G.E., Mickel, W., Kapfer, S.C., Klatt, A., Schaller, M., Hoffmann, M., Kleppmann, N., Armstrong, P., Inayat, A., Hug, D., Reichelsdorfer, M., Peukert, W., Schwiager, W., Mecke, K., 2011. Minkowski Tensor Shape Analysis of Cellular, Granular and Porous Structures. *Advanced Materials* 23, 2535–2553. doi:10.1002/adma.201100562.
- [71] Schümann, M., Odenbach, S., 2021. The Microstructure of Magnetorheological Materials Characterized by Means of Computed X-Ray Microtomography. *Physical Sciences Reviews* doi:10.1515/psr-2019-0105. publisher: De Gruyter.
- [72] Seibert, P., Ambati, M., Raßloff, A., Kästner, M., 2021. Reconstructing random heterogeneous media through differentiable optimization. *Computational Materials Science* 196, 16.
- [73] Seibert, P., Raßloff, A., Ambati, M., Kästner, M., 2022a. Descriptor-based reconstruction of three-dimensional microstructures through gradient-based optimization. *Acta Materialia* 227, 117667. URL: <https://linkinghub.elsevier.com/retrieve/pii/S1359645422000520>, doi:10.1016/j.actamat.2022.117667.
- [74] Seibert, P., Raßloff, A., Kalina, K., Ambati, M., Kästner, M., 2022b. Microstructure Characterization and Reconstruction in Python: MCRpy. *Integrating Materials and Manufacturing Innovation* 11, 450–466. URL: <https://link.springer.com/10.1007/s40192-022-00273-4>, doi:10.1007/s40192-022-00273-4.
- [75] Seibert, P., Raßloff, A., Kalina, K.A., Gussone, J., Bugelnig, K., Diehl, M., Kästner, M., 2023. Two-stage 2D-to-3D reconstruction of realistic microstructures: Implementation and numerical validation by effective properties. *Computer Methods in Applied Mechanics and Engineering*.
- [76] Sidhu, S.S., 1995. Elliptic integrals and functions. *Computers in Physics* 9, 268–276.
- [77] Tian, T.F., Li, W.H., Deng, Y.M., 2011. Sensing Capabilities of Graphite Based MR Elastomers. *Smart Materials and Structures* 20, 025022.

- [78] Vlassis, N.N., Sun, W., 2021. Sobolev training of thermodynamic-informed neural networks for interpretable elasto-plasticity models with level set hardening. *Computer Methods in Applied Mechanics and Engineering* 377, 113695. URL: <https://www.sciencedirect.com/science/article/pii/S0045782521000311>, doi:10.1016/j.cma.2021.113695.
- [79] Volkova, T., Böhm, V., Kaufhold, T., Popp, J., Becker, F., Borin, D., Stepanov, G., Zimmermann, K., 2016. Motion Behaviour of Magneto-Sensitive Elastomers Controlled by an External Magnetic Field for Sensor Applications. *Journal of Magnetism and Magnetic Materials* doi:<http://dx.doi.org/10.1016/j.jmmm.2016.10.009>.
- [80] Wei, L.Y., Lefebvre, S., Kwatra, V., Turk, G., 2009. State of the Art in Example-based Texture Synthesis. *Eurographics 2009, State of the Art Report, EG-STAR*, 93–117.
- [81] Xu, H., Dikin, D.A., Burkhart, C., Chen, W., 2014. Descriptor-based methodology for statistical characterization and 3D reconstruction of microstructural materials. *Computational Materials Science* 85, 206–216. doi:10.1016/j.commatsci.2013.12.046.
- [82] Yeong, C.L.Y., Torquato, S., 1998. Reconstructing random media. *Physical Review E* 57, 495–506. doi:10.1103/PhysRevE.57.495.
- [83] Zhang, F., Teng, Q., Chen, H., He, X., Dong, X., 2021. Slice-to-voxel stochastic reconstructions on porous media with hybrid deep generative model. *Computational Materials Science* 186, 110018. doi:10.1016/j.commatsci.2020.110018.
- [84] Zhang, Y., Seibert, P., Otto, A., Raßloff, A., Ambati, M., Kastner, M., 2023. DA-VEGAN: Differentiably Augmenting VAE-GAN for microstructure reconstruction from extremely small data sets .
- [85] Zhu, C., Byrd, R.H., Lu, P., Nocedal, J., 1997. Algorithm 778: L-BFGS-B: Fortran subroutines for large-scale bound-constrained optimization. *ACM Transactions on Mathematical Software* 23, 550–560. URL: <http://portal.acm.org/citation.cfm?doid=279232.279236>, doi:10.1145/279232.279236.